remote sensing

MDPI

Article

Comparison of Crustal Stress and Strain Fields in the Himalaya–Tibet Region: Geodynamic Implications

Federico Pietrolungo [1,2,3,*], Giusy Lavecchia [2,3], Asier Madarieta-Txurruka [4,5], Federica Sparacino [1], Eshaan Srivastava [5], Daniele Cirillo [2,3], Rita de Nardis [2,3], Carlo Andrenacci [3,6], Simone Bello [2,3,7], Nicolò Parrino [5], Attilio Sulli [5] and Mimmo Palano [1,5,8]

1 Istituto Nazionale di Geofisica e Vulcanologia, Osservatorio Etneo—Sezione di Catania, Piazza Roma 2, 95123 Catania, Italy; federica.sparacino@ingv.it (F.S.); mimmo.palano@unipa.it (M.P.)
2 Dipartimento di Scienze, Università degli Studi "G. d'Annunzio", Via dei Vestini 31, 66100 Chieti, Italy; glavecchia@unich.it (G.L.); d.cirillo@unich.it (D.C.); rita.denardis@unich.it (R.d.N.); simone.bello@unich.it (S.B.)
3 Centro inteRUniversitario per l'analisi Sismotettonica Tridimensionale (CRUST), 66100 Chieti, Italy; carlo.andrenacci@unich.it
4 Departamento de Geología, Universidad del País Vasco/Euskal Herriko Unibertsitatea, Barrio Sarriena s/n, 48940 Leioa, Spain; asier.madarieta@ehu.eus
5 Dipartimento di Scienze della Terra e del Mare, Università degli Studi di Palermo, Via Archirafi 22, 90123 Palermo, Italy; eshaan.srivastava@unipa.it (E.S.); nicolo.parrino@unipa.it (N.P.); attilio.sulli@unipa.it (A.S.)
6 Istituto Nazionale di Geofisica e Vulcanologia, Sezione di Roma 1, Via di Vigna Murata, 605, 00143 Rome, Italy
7 Istituto di Geologia Ambientale e Geoingegneria, Consiglio Nazionale delle Ricerche (CNR-IGAG), Area della Ricerca di Roma 1, Strada Provinciale 35d, 9, 00010 Montelibretti, Italy
8 Istituto di Geologia Ambientale e Geoingegneria, Consiglio Nazionale delle Ricerche (CNR-IGAG), P.le A. Moro, 5, 00185 Rome, Italy
* Correspondence: federico.pietrolungo@unich.it

Abstract: The Himalaya–Tibet region represents a complex region of active deformation related to the ongoing India–Eurasia convergence process. To provide additional constraints on the active processes shaping this region, we used a comprehensive dataset of GNSS and focal mechanisms data and derived crustal strain and stress fields. The results allow the detection of features such as the arc-parallel extension along the Himalayan Arc and the coexistence of strike-slip and normal faulting across Tibet. We discuss our findings concerning the relevant geodynamic models proposed in the literature. While earlier studies largely emphasized the role of either compressional or extensional processes, our findings suggest a more complex interaction between them. In general, our study highlights the critical role of both surface and deep processes in shaping the geodynamic processes. The alignment between tectonic stress and strain rate patterns indicates that the crust is highly elastic and influenced by present-day tectonics. Stress and strain orientations show a clockwise rotation at 31°N, reflecting deep control by the underthrusted Indian Plate. South of this boundary, compression is driven by basal drag from the underthrusting Indian Plate, while northward, escape tectonics dominate, resulting in eastward movement of the Tibetan Plateau. Localized stretching along the Himalaya is likely driven by the oblique convergence resulting from the India–Eurasia collision generating a transtensional regime over the Main Himalayan Thrust. In Tibet, stress variations appear mainly related to changes in the vertical axis, driven by topographically induced stresses linked to the uniform elevation of the plateau. From a broader perspective, these findings improve the understanding of driving crustal forces in the Himalaya–Tibet region and provide insights into how large-scale geodynamics drives surface deformation. Additionally, they contribute to the ongoing debate regarding the applicability of the stress–strain comparison and offer a more comprehensive framework for future research in similar tectonic settings worldwide.

Keywords: focal mechanisms; stress field; GNSS velocity; strain rate; Himalaya–Tibet; geodynamic models

Citation: Pietrolungo, F.; Lavecchia, G.; Madarieta-Txurruka, A.; Sparacino, F.; Srivastava, E.; Cirillo, D.; de Nardis, R.; Andrenacci, C.; Bello, S.; Parrino, N.; et al. Comparison of Crustal Stress and Strain Fields in the Himalaya–Tibet Region: Geodynamic Implications. *Remote Sens.* **2024**, *16*, 4765. https://doi.org/10.3390/rs16244765

Academic Editor: Antonio Miguel Ruiz Armenteros

Received: 8 November 2024
Revised: 16 December 2024
Accepted: 19 December 2024
Published: 20 December 2024

1. Introduction

The spatial comparison of crustal stress and strain patterns is one of the most compelling approaches in a geodynamically complex framework. It provides useful constraints on driving forces and highlights those regions which accumulate stress and encourage seismic deformation. This approach has been widely applied in the literature to describe crustal behavior and deformation models [1–6]. For instance, Chang et al. [6], studying Taiwan Island, found that both stress and strain fields perceptively reflect the long-term collision mechanism and that inherited structure can play a role in redirecting the stress–strain orientation. In Japan, Townend and Zoback [5] found that observed geodetic velocities are mainly driven by the crustal collision rather than the subduction zone locking; Palano et al. [2] applied the comparison to the Gibraltar Orogenic Arc, finding a significant coherence between well-constrained stress indicators and GNSS-derived strain, therefore suggesting that deep dynamic processes control both crustal stress and surface deformation. Other studies have been conducted both in geothermal-active regions [7] and in volcanically active areas [4], providing information on the seismicity distribution and deformation behavior of these areas.

Himalaya–Tibet (Figure 1) represents a complex region of active deformation related to the long-lasting and still active India–Eurasia convergence process [8]. Although the Indian-Eurasian convergence is a puzzling geodynamic process that generates active deformation and seismicity across different geographical areas, such as the Kachchh region [9–12], most of the crustal deformation is currently concentrated along the Himalayan Arc, driven by the high convergence rate between the Indian and Eurasian Plates [13]. In the central sector of the Himalayan Arc (Nepal), the convergence is predominantly arc-normal [14,15], while to the east and west, a significant arc-parallel component of deformation has been observed both by geological and geodetic data [16–21]. Despite the ongoing N–S convergence, southern and central Tibet are also experiencing significant E–W extension. This complex structural configuration, characterized by the concurrent presence of active strike-slip and normal fault systems traversing Tibet [22,23], hampers effective kinematic zonation in the region that still lack definitive characterization.

Due to its complexity, different models have been proposed for the ongoing deformation (at least for the last few Ma) of the Himalaya–Tibet region: the topographic loading [24], the *indenter-escape tectonic* [25], the *thinning model* [21], the *oblique convergence* [26], and the *channel flow* [27].

We employ the latest and most comprehensive geodetic crustal motion data, along with a novel estimation of the seismological stress and geodetic strain rate fields. Using these results, we aim to furnish a critical bridge among current geodynamic models proposed for the Himalaya–Tibet region, providing therefore an empirical evaluation of their applicability through a detailed stress–strain comparison. Such a detailed comparison will offer a refined perspective on ongoing tectonic processes, enhancing understanding of the driving forces behind crustal deformation in complex tectonic settings.

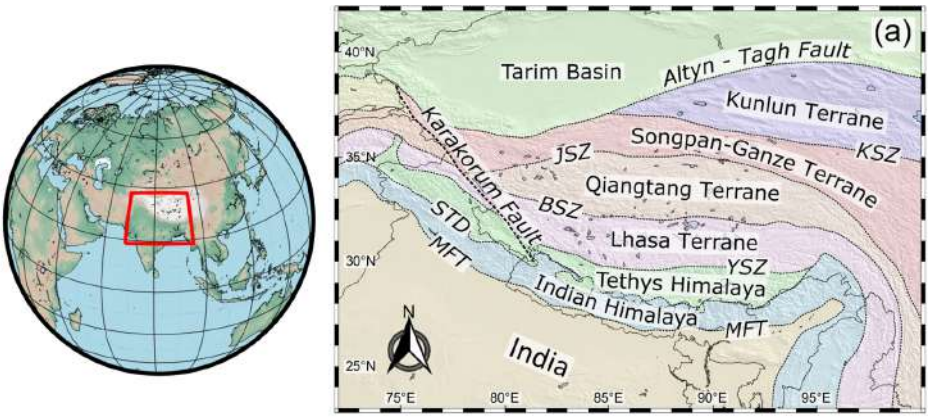

Figure 1. *Cont.*

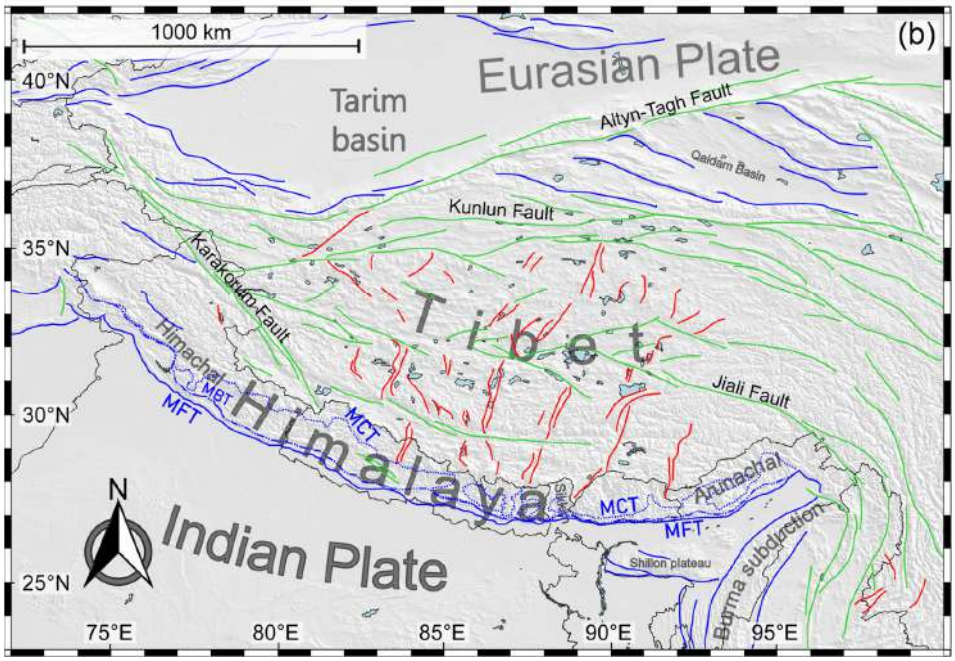

Figure 1. Geological background of the Himalaya–Tibet region. (**a**) Main terranes, suture zones and principal tectonic lineaments on the study region (modified from Li et al. [28]). KSZ—Kunlun Suture Zone, JSZ—Jinsha Suture Zone, BSZ—Bangong-Nujiang Suture Zone, YSZ—Yarlung-Tsangpo Suture Zone, STD—South Tibetan Detachment, MFT—Main Frontal Thrust. (**b**) Active and main faults from Zelenin et al. [29]: blue: thrust; red: normal fault; green: strike-slip fault. MCT—Main Central Thrust, MBT—Main Boundary Thrust, MFT—Main Frontal Thrust. The terrain model is from GEBCO [30], accessed on 31 October 2024.

2. Background

2.1. Geodynamic Evolution

Tibet (i.e., the region in central Asia located between the Tarim Basin to the north and the Indian Plate to the south) has an extensive geological history [8]. The current geological setting of Tibet resulted from the occurrence of sequential geodynamic events such as microcontinent collision, the building of orogenic belts, and the formation of island arcs, at least since the early Paleozoic [31]. Nowadays, from north to south, the Kunlun (KUT), Songpan-Ganze (SGT), Qiangtang (QT), Lhasa (LHT), the Tethys Himalaya (THT), and the Indian Himalaya (INT) terranes represent the pronounced horizontal heterogeneity of the plateau [19] (Figure 1a). These terranes are separated by suture zones, including the Kunlun (KSZ), Jinsha (JSZ), Bangong-Nujiang (BSZ), and Yarlung-Tsangpo sutures (YSZ) (Figure 1a). All these suture lines are the result of a succession of subductions, from the closure of the Paleo-Tethys in the Late Triassic (Kunlun and Jinsha suture zones) up to the closure of the Bangong-Nujiang Ocean, the northern branch of the Neo-Tethys, with the formation of the Bangong-Nujiang suture zone in the Late Cretaceous [32].

Since the Late Cretaceous, India began its northward drift, separating Gondwana. During this process, the Tethys Himalaya Terrane moved away from India, leading to the opening of the North Indian Sea. Both India and the Tethys Himalaya moved towards the Eurasian plate at a rate of approximately 15–18 cm/yr until they collided around 60–55 Ma [8]. Around 50 Ma, the convergence rates significantly slowed to 6 cm/yr, marking the onset of the continent–continent collision phase [33]. This latest phase of shortening has been accommodated by the continuous underthrusting of the Indian shield beneath the Tethyan Himalaya and the Lhasa Terrane [34], as also evidenced by recent seismic observations [35] which imaged a distinct cold body beneath the Lhasa Terrane. The underthrusting also explains the uplift in Tibet during the last 40 Ma [36,37]. However, other hypotheses have been suggested [38–40].

Following the India–Eurasia collision, the deformation fronts progressively shifted southward from the YSZ, giving rise to the imbricated fold-and-thrust belt of the Himalayas. Southward, Tibet is bounded by the South Tibetan Detachment (STD), which represents the lower boundary of the stacked Tethyan Himalaya sequence. The STD is a lithospheric shear zone in which both reverse and normal faulting episodes have been recorded [39–41]. The detachment acted as a shortening structure during the Eocene [42], meanwhile the normal faulting was probably active during the Miocene [43]. Different hypotheses have been proposed for the reactivation of the STD with normal faulting features [44] such as gravitational collapse [45], wedge extrusion [46], channel flow [47], or tectonic wedging/duplexing [48,49].

In the southern part of the STD, the Indian Himalaya Terrane is affected by a complex thrust system formed by the Main Central Thrust (MCT), the Main Boundary Thrust (MBT), and the Main Frontal Thrust (MFT). While activity on the MCT started around ~22–18 Ma and may have remained episodically active up to the present day [50,51], the MBT developed from 11 Ma until the Pleistocene. The MFT defines the southernmost margin of the orogenic arc and represents the near-surface expression of the deep basal décollement (Main Himalayan Thrust; hereinafter, MHT). The MHT separates the Indian shield from the Indian Himalaya terrane and is currently acting as the gently inclined basal detachment with a ramp-flat geometry underlying this complex structure [16]. The MHT appears to be segmented by subsurface transverse tectonic lineaments and faults, with normal to strike-slip features in regions with low seismic coupling values [50]. These regions are marked at depth by the presence of subsurface paleo-basement ridges, such as the Delhi–Haridwar (DHR), the Faizabad (FR) and the Munger–Saharsa (MSR) [52].

2.2. Seismotectonic Framework

Past seismic activity highlights the Himalaya–Tibet region as an area of high seismic risk, with numerous moderate-to-large earthquakes ($6 < M_w < 7$) distributed across the region [53]. By inspecting the USGS catalog (https://earthquake.usgs.gov, accessed on 31 May 2024), ~15,000 earthquakes with $M_w > 2.5$ spanning the 1960–March 2024 time interval have been selected (Figure 2). Despite being one of the most seismically active regions in the world, instrumental hypocenters in the area are poorly constrained due to the lack of local seismic networks, especially in Tibet. Instrumental seismicity occurs within approximately 100 km of the Main Himalayan Thrust (MHT) downdip, with notable seismic gaps in Bhutan [54]. In more detail, it is sparsely distributed in a clustered pattern along the collisional arc, following some of the strike-slip lineaments and in a N–S aligned pattern around a few normal faults. It is also primarily concentrated within the upper 30–35 km of the crust, though intermediate-depth (>40 km [55]) seismic events have been locally recorded beneath the Himalayas [30]. In the last century, Himalaya has experienced four large seismic events ($M_w > 7$) such as the M_w 8.9 1950 Assam earthquake [56,57], the M_w 7.8 and M_w 7.3 2015 Gorkha [58,59], and the M_w 7.6 2005 Kashmir ones [60].

The southern border of Tibet is currently experiencing a marked E-W crustal stretching, which is accommodated by N-S-oriented normal [61] and active strike-slip faults [61,62]. These active faults are associated with widespread seismicity with $M_w > 6$, e.g., the M_w 6.2 2004 and the M_w 6.3 2005 Zhongba earthquakes [63], the M_w 6.3 2008 Damxung earthquake [64], and the M_w 6.1 2020 Nima earthquake [65], also including notable seismic sequences. Strike-slip faults, predominantly oriented NW-SE or NE-SW, have generated several significant seismic events, including the M_w 7.7 1951 Beng Co earthquake [66], the M_w 6.9 2014 Yutian earthquake [67], and the M_w 7.6 2001 Kunlun earthquake [68].

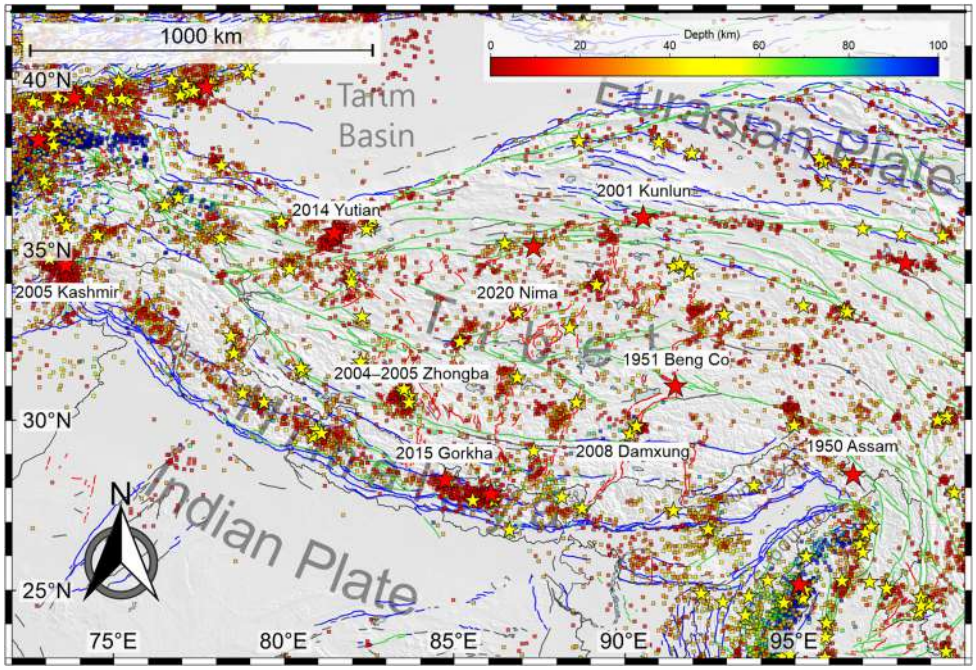

Figure 2. Instrumental seismicity (M_w > 2.5) from 1960 to 2024 (USGS catalog; https://earthquake.usgs.gov (accessed on 31 May 2024)), colored according to focal depth with a rainbow color scale. Yellow and red stars are seismic events with 6 < $M_w \leq 7$ and M_w > 7, respectively. Earthquakes before 1960 (1950 Assam and 1951 Beng Co) are from Coudurier-Curveur et al. [56] and Li et al. [66], respectively. Active and main faults from Zelenin et al. [29]: blue: thrust; red: normal fault; green: strike-slip fault; gray: unknown kinematic fault. The terrain model is from GEBCO [30], accessed on 31 October 2024.

2.3. Geodynamic Models

Several geodynamic models have been proposed to explain the complex fragmentation and kinematic heterogeneity of the Himalaya–Tibet region. All models primarily aim to interpret the synchronous coexistence of (i) a roughly N-S striking compression, as resulting from the collisional process between Indian and Eurasian plates, with (ii) an E–W extension, related to a general eastward motion of Tibet.

N-S trending normal faults in Tibet are commonly thought to represent the active deformation due to *topographic loading* [24,69,70]. Collapse occurs in response to the isostatic compensation in the highly thickened Tibetan crust (~70 km [71]). The *topographic loading* model is only able to explain extension in the Tibet region, without fully accounting for the eastward motion of all the Tibetan terranes and the distributed active strike-slip faults.

Tapponier and Molnar [25] explain the eastward motion of Tibet by suggesting an *indenter-escape tectonic model*. According to this model, the weak Tibetan lithosphere is tectonically pushed eastward because of the N-S convergence of the highly rigid lithosphere of India and the Tarim Basin (Eurasia). The indenter block was too buoyant to subduct, so lithospheric accommodation is mainly achieved by the eastward extrusion of Tibet. This model well explains the clockwise rotation of eastern Tibet [72] and the bending of faults such as the Jiali Fault [73]. However, the *indenter-escape tectonic model* assumes that deformation is mainly confined to the horizontal plane, neglecting vertical deformations, which would be relevant, especially in the Himalaya–Tibet region where the crust is the thickest in the world. Furthermore, such an explanation is insufficient as it considers extensional tectonics isolated from the compressive forces arising from the ongoing India–Eurasia convergence. These compressive forces would be crucial in driving the uplift of the plateau from the Paleogene up to the present, as testified by the ongoing uplift inferred by recent leveling and GNSS measurements [37].

A primary piece of information for enhancing the understanding of the active geodynamics of the Himalaya–Tibet region is the precise location of the Indian Plate beneath Tibet. A gently northward-dipping surface has been presented by different authors [35,74–77], revealing similar seismic characteristics of the layers up to 31°N. The presence of the underthrusted Indian crust has led to the proposal of two additional models closely related to the active dynamics.

The *thinning model* [21] suggests that the subsequent extension reflects the thinning of the upper crust in response to thickening due to the underthrusted Indian Plate. This model has two significant limitations: (i) extension does not cease at 31°N but also affects the Qiangtang Terrane and (ii) while extension should theoretically activate progressively from south to north, it appears to have started fairly uniformly across the plateau during the Miocene [69,78].

Beyond that, other authors have proposed the oblique convergence model [26,79–81] which also assumes the underthrusting of India but explains the extension through the relative movement between the Indian and Eurasian plates. McCaffrey and Nábělek [26] observed that the former plate moves as a whole towards the north, evidencing that the convergence is perpendicular only in a limited sector of the Himalayas, having its contact zone with the Eurasian Plate in a semicircular shape. Such a feature highlights that in the other sectors, the overall convergence is also partitioned into a parallel component. In such a context, the E-W extension would result from a basal shear caused by the Indian oblique underthrusting beneath Tibet. However, this model is unable to properly explain the deformation northward of the underthrusted Indian Plate, as similarly observed for the thinning model. Additionally, this model requires higher deformation values moving west and south where, according to some authors (e.g., [31]), the convergence is less perpendicular and shallower, with the maximum rates occurring in the western Himalayan region.

An additional attempt to explain the complexity of deformation was the channel flow model by Bird [27]. This author was the first to theorize, through numerical models, the possible presence of a deep zone in the Tibetan crust hosting a planar channel flow. Beaumont et al. [82], using thermal-mechanical models, explain that the effect of surface denudation could be due to crustal channel flow which, as also noted by Colpey and McKenzie [83], causes the Himalayan Arc to expand both radially and circumferentially. Rey et al. [84] suggested that the critical thickness required to weaken the lower crust would be 50 km, raising the question of how a real thickness of ~70 km [71] could be attained. In this context, the observed uplift may be difficult to explain since the channel flow model is typically considered a consequence of uplift rather than its cause [84].

3. Data

3.1. GNSS Data

As a first step, raw observations of more than 150 continuous GNSS stations encompassing the Himalaya–Tibet region were collected from UNAVCO (https://www.unavco.org (accessed on 31 May 2024)). After a preliminary check, 37 stations were removed because they were characterized by a limited temporal coverage of raw data (less than 2.5 years), while the remaining stations were processed by using the GAMIT/GLOBK v.10.7 software [85], following the standard approach described in Billi et al. [86], in order to estimate a consistent set of positions and velocities in a fixed ITRF14 reference frame [87]. To enhance the spatial density of the geodetic velocity field across the studied area, the obtained solution has been integrated with the solutions reported in the recent literature [88–90]. Published solutions were aligned with our solution by determining the Helmert transformation parameters that minimize the root mean square of velocity differences at common sites (e.g., [91]). All sites displaying significant inconsistencies with neighboring stations were removed from the unified velocity field, resulting in a final dataset of approximately 1142 GNSS sites. The resulting velocity field (Figure 3) has been rotated to an Eurasian reference frame by using the Euler pole parameters reported in Altamimi et al. [92].

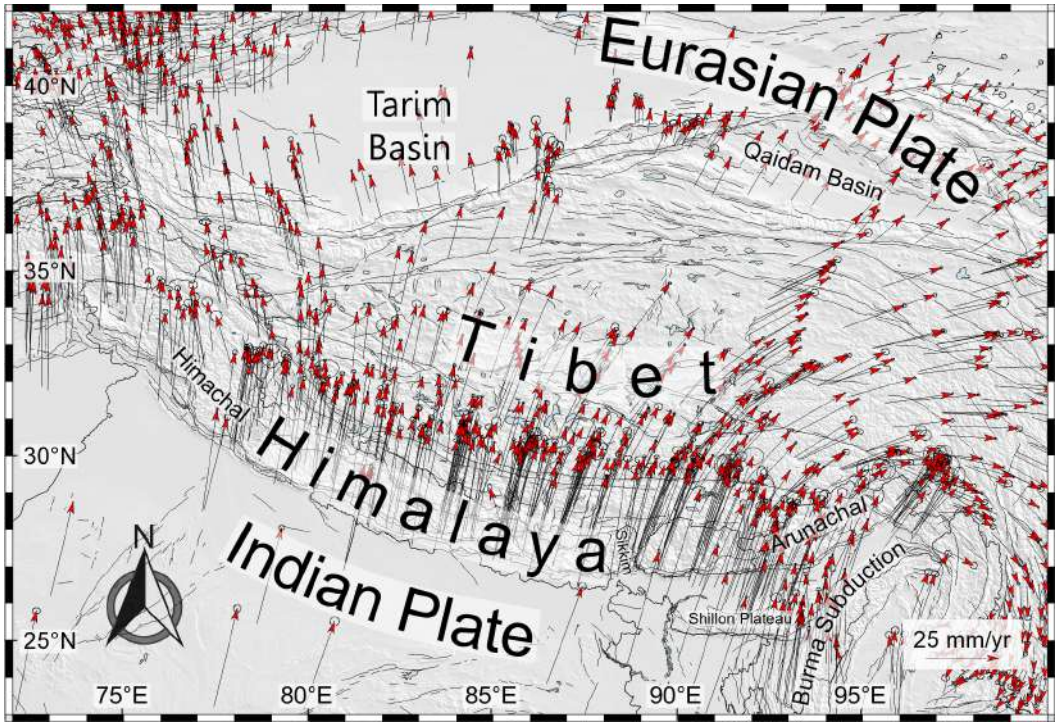

Figure 3. Thin red head arrows represents the GNSS horizontal velocities and 95% confidence ellipses in an Eurasian reference frame [92]. The terrain model is from GEBCO [30], accessed on 31 October 2024.

3.2. Seismicity and Focal Mechanisms Catalog

Mechanical stress acting in the Earth's crust can be estimated by inverting earthquake focal mechanisms. Therefore, to provide a reliable estimation of the crustal stress in the study area, a dataset of FMSs has been compiled. In a first step we collected all available FMSs over the Himalaya–Tibet area by inspecting the following sources:

- GCMT (https://www.globalcmt.org/ accessed on 31 May 2024);
- ISC (http://www.isc.ac.uk/iscgem/index.php accessed on 31 May 2024);
- World Stress Map [93] (https://www.world-stress-map.org/download accessed on 31 May 2024).

Multiple solutions for the same event have been removed, selecting the solution having the least difference concerning the hypocentral parameters reported in the USGS seismic catalog (Figure 2).

In the second step, data from the literature have been integrated into the general catalog by preferring the solutions coming from local seismic networks or computed by using refined velocity models [52,94–111]. Moreover, since the procedure of the waveform-inversion FMSs is generally more stable and robust than solutions obtained by first-motion polarity (e.g., [112,113]), the former was selected when both types of solutions were available for the same earthquake.

The final catalog contains ~1300 FMSs related to $M_w > 4$ earthquakes that occurred in the June 1933–March 2024 period (Figure 4). About ~80% of the collected FMSs have been obtained by waveform inversion, while the remaining has been computed by first-motion polarity and are related to the earthquakes that occurred before the advent of the digital epoch in the 1980s. In the study area, most of the FMSs have focal depths less than 30 km; ~8% have focal depths up to 80 km. Among these last solutions, the most remarkable ones are those related to the 2011 Sikkim seismic sequence [114] that occurred beneath the MHT, and those related to the Burma active subduction and the Pamir–Hindu Kush lithospheric subduction [115].

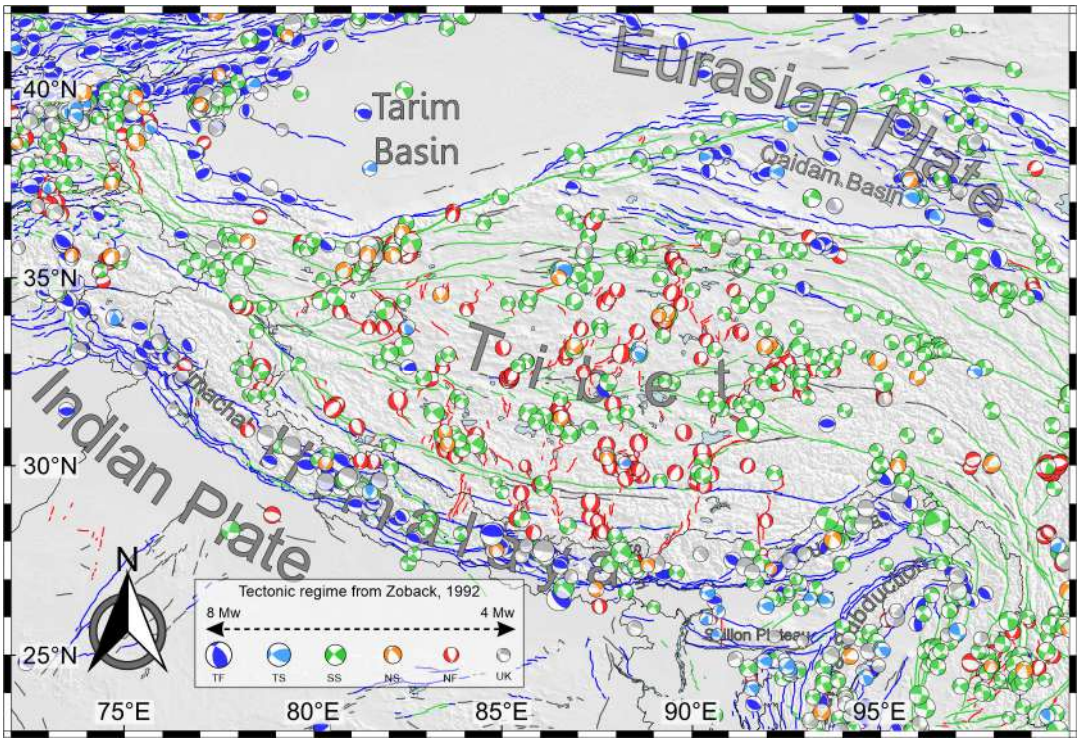

Figure 4. Lower hemisphere, equal area projection for FMSs with M > 4 spanning the June 1933–February 2024 time period. FMSs are colored according to kinematic classification [116]: blue: thrust faulting (TF); light blue: thrust with strike-slip component (TS); green: pure strike-slip (SS); orange: normal faulting with strike-slip component (NS); red: normal faulting (NF); gray: unknown kinematics (UK). Other features are as Figure 2. The terrain model is from GEBCO [30], accessed on 31 October 2024.

4. Method

4.1. Geodetic Strain Rate Field

The horizontal strain rate pattern and associated uncertainties over the study area have been calculated using the method described by Shen et al. [117]. This algorithm employs discretized geodetic observations and applies a least-squares procedure to interpolate velocities on an optimally regular grid. Interpolated velocities are then used to derive strain rate values by assuming the medium to be elastic. After some preliminary tests, we chose a value of 18 as the weighting threshold, according to the inter-stations distance of the GNSS network [118] and the comparative analysis conducted by Nucci et al. [119].

This study examines the minimum and maximum stretching, ε_{Hmin} and ε_{Hmax}, respectively, as eigenvalues of the computed strain rate tensor, alongside their corresponding azimuths. The two eigenvectors are assumed to be orthogonal to each other and oriented at 45° relative to the azimuth of the maximum shear strain. Additionally, a crucial parameter is the dilatation strain rate, which quantifies the rate of the areal change as the sum of the ε_{Hmin} and ε_{Hmax} values.

The adopted grid nodes are evenly spaced at intervals of 0.25° × 0.25°. The distribution of stations across the area is irregular (Figure 3); therefore, the results for these regions, such as north–central Tibet and the Tarim Basin, must be interpreted keeping this aspect in mind. Achieved results are reported in Figure 5.

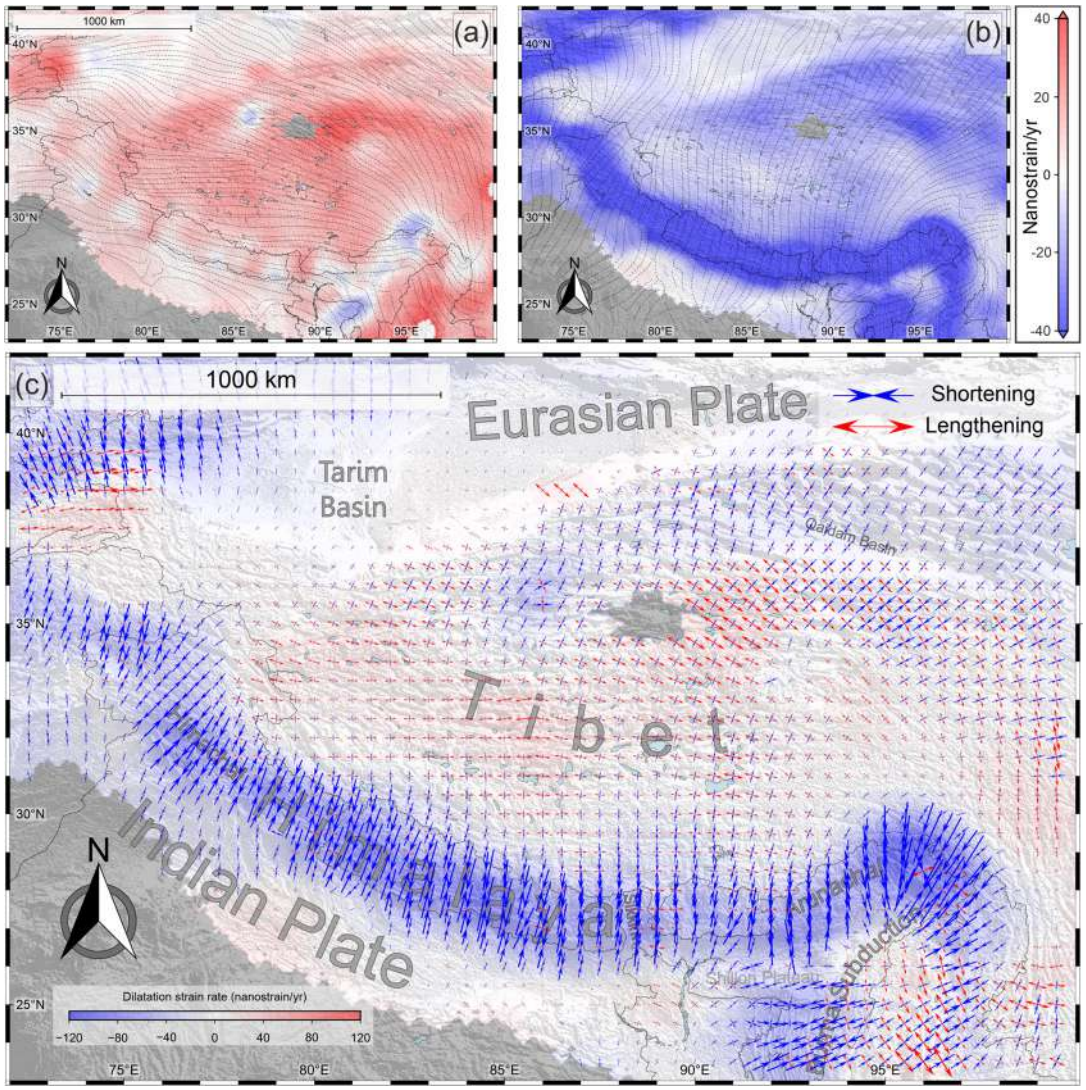

Figure 5. Strain rate maps from GNSS data. (**a**) ε_{Hmax} (greatest extensional horizontal strain rate) trajectories are reported as dotted black lines. The background color indicates the magnitude of ε_{Hmax}: negative and positive values for shortening and lengthening, respectively. (**b**) ε_{Hmin} (greatest contractional horizontal strain rate) trajectories are reported as dotted black lines. The background color is the same as (**a**). (**c**) Horizontal strain rate axes; red and blue arrows represent the greatest extensional (ε_{Hmax}) and contractional (ε_{Hmin}) horizontal strain rates. The colors in the background show the 2D dilatation strain rate, blue and red for areal contraction and dilatation, respectively. The terrain model is from GEBCO [30], accessed on 31 October 2024.

4.2. FMS Formal Inversion

The stress tensor over the study area has been calculated by using the FMSs database (see Section 3.2) fusing of the STRESSINVERSE code ($M_w > 4$ earthquakes) [120] as the input. This code calculates the stress tensor parameters assuming: (i) the tectonic stress is uniform and homogeneous in the considered volume, (ii) earthquakes occur on pre-existing faults, and (iii) the slip vector points to the direction of shear stress on the fault [120–122]. This method can determine the 3D stress tensor, defining trend, and plunge of the three axes, σ_1, σ_2, and σ_3 (with $\sigma_1 \geq \sigma_2 \geq \sigma_3$, under the compression-positive stress convention), and the dimensionless stress ratio, R [123]:

$$R = \frac{\sigma_1 - \sigma_2}{\sigma_1 - \sigma_3} \quad (1)$$

The stress ratio R varies from 0 to 1.0; when R = 0, σ_1 and σ_2 are equal in magnitude, while R = 1 means that σ_2 and σ_3 have the same values.

To ensure more accurate estimations of stress ratio values, the STRESSINVERSE code selects the optimal nodal plane [120] by quantifying the fault instability [124], following the Mohr–Coulomb failure criterion [125]. To properly evaluate the sensitivity of the inversion procedure to friction parameters, needed in the instability constraint, the inversion was run repeatedly with friction ranging from 0.4 to 1 in steps of 0.05. Thus, the code performs a set of iterations aimed at determining the orientation of the stress axes and the estimation of the stress ratio, considering all possible nodal plane combinations, until the stress parameters converge toward the best model [126]. In this way, the instability of the nodal planes of all FMSs is calculated, selecting those most susceptible to shear faulting.

The inversion has been performed on a moving 2° × 2° equally spaced grid with a 1° overlap on each side. The inversion is only performed in cells containing at least 8 FMSs. Based on the measured stress field geometry and stress ratio, the so-called maximum sub-horizontal compressive stress, σ_{Hmax}, is also calculated [127] (see Figure 6a).

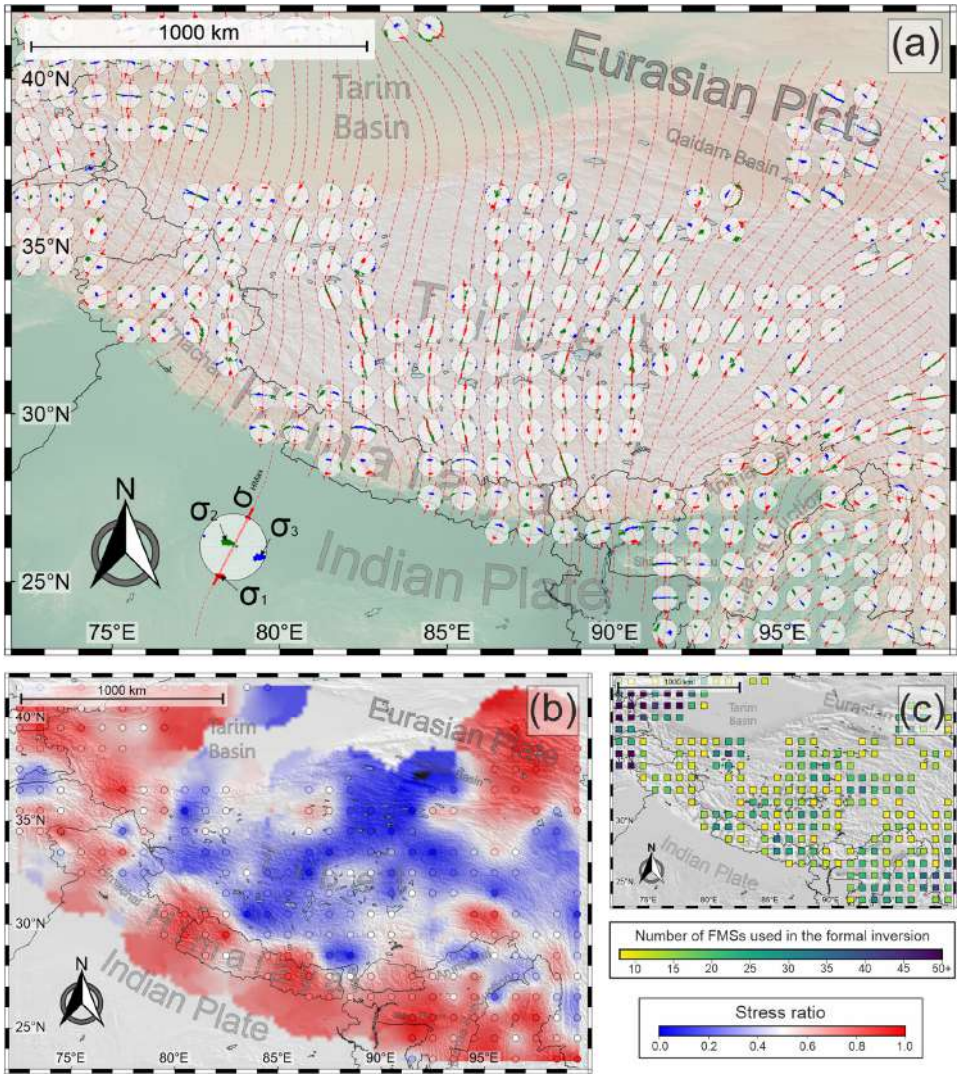

Figure 6. Results from formal stress inversion (**a**) Stereoplots (lower hemisphere) showing achieved results. σ_1, σ_2, and σ_3 axes are reported in red, green, and blue, respectively. The σ_{Hmax} trajectories are reported as red dashed lines. (**b**) Spatial pattern of the stress ratio values. (**c**) Colored squares showing the number of FMSs used in the gridded stress inversions. The terrain model is from GEBCO [30], accessed on 31 October 2024.

5. Results

5.1. Strain Rate Field

Strain rate results are reported in Figure 5 as ε_{Hmax} and ε_{Hmin} values along with the associated azimuthal pattern (i.e., arrows and trajectories). Despite some very localized artifacts, our results align well with previous solutions [89,128], providing, moreover, an improved resolution of the deformation field thanks to the high spatial density of the geodetic velocity field across the studied area.

The ε_{Hmax} strain parameter has positive values with very small variability over most of the study area. The largest positive values (up to 30 nanostrain/yr) are observed in the entire of Tibet, while values ranging from 0 to ~25–30 nanostrain/yr can be observed along six localized N-S oriented strips along the Himalayan Arc. Some small patches with negative values (~25 nanostrain/yr) can be observed close to Arunachal, the Shillong plateau, and the Himachal regions. The ε_{Hmax} trajectories outline a general E-W trend, gradually rotating, moving eastward. Along the Himalayan Arc, the ε_{Hmax} trajectories pass from a roughly WNW-ESE attitude in the western Himalaya to E-W and N-S attitudes in central and eastern Himalaya (Figure 5a).

The ε_{Hmin} values effectively depict the general contraction of the study areas, with low values (ca. −25 nanostrain/yr) mainly characterizing the Tibetan region and high values along the Himalayan Arc (up to −100 nanostrain/yr) and at the northern margin of Tibet, along the Altyn-Tagh and Kunlun faults (up to −40 nanostrain/yr). The ε_{Hmin} trajectories show a general NNE-SSW trend over most of the study area. Such a pattern is roughly orthogonal to the general attitude of the Himalayan Arc. A marked rotation is observed in proximity to the Arunachal area, where the ε_{Hmin} trajectories follow the clockwise rotation of the orogenic belt, aligning NE-SW. Another interesting feature is the gradual rotation of the ε_{Hmin} trajectories observed in the Tibetan Plateau. In the southern part of the plateau, the ε_{Hmin} trajectories show a predominant N-S orientation, while north of the 31°N parallel, the trajectories gradually rotate clockwise about 30°. The horizontal dilatation rate map (sum of ε_{Hmin} and ε_{Hmax}) is dominated by the contractional pattern (up to −120 nanostrain/yr) along the Himalayan orogen, clearly evidencing the ongoing India–Eurasia convergence. Such a general contraction concentrated within 100 km north of the MFT indicates the active contraction of the Indian Himalaya above the MHT. In the Tibetan region, the areal change values are close to zero or show small local variations, indicating no significant change in areal strain. However, given that ε_{Hmax} and ε_{Hmin} have similar (not zero) values, it can be inferred that crustal deformation in the Tibetan region occurs prevalently as shear strain, in a generally constant area strain in the map view [129]. Such a feature aligns well with the presence of abundant strike-slip faults, responsible for several large earthquakes. The dilatation rate is close to zero in the Tarim Basin where, in contrast to Tibet's results, ε_{Hmin} and ε_{Hmax} have very small or close to zero values, suggesting a small/null deformation of the region. Estimated strain rate parameters over this area would be poorly constrained because of the lack of GNSS stations; however, the small/null deformation within the Tarim Basin is also confirmed by geological data, clearly documenting no active deformation since the onset of the India–Eurasia convergence [130,131]. Moreover, both the southern and northern margins of the Tarim Basin show negative areal changes that appear related to the presence of active faults/structures, such as the Altyn Tagh fault and the Tianshan orogeny, respectively.

5.2. Stress Field

The estimated stress parameters over the study area are reported in Figure 6 (see Supplementary Material for additional details). As already mentioned, most of the collected FMSs are related to earthquakes located in the uppermost part of the crust, within the first 30–35 km. Therefore, our stress results must be considered as representative only of the shallow crust, being the average crustal thickness of ~70 km [71] beneath most of the study area. Figure 6a shows achieved results for each inverted cell in terms of stereoplot representations and stress trajectories. As mentioned previously, the stress tensor inversion

has been performed only for those cells containing at least eight FMSs. Only a few cells contain eight FMSs, and their resulting stress parameters agree with the ones obtained for the neighboring cells, evidencing acceptable reliability of the estimations. Each stereoplot shows the retrieved principal stress (σ_1, σ_2 and σ_3) 3D spatial pattern along with the associated confidence limits, while the stress trajectories refer to the σ_{Hmax} pattern.

Along the Himalayan Arc, the σ_1 stress axis is roughly sub-horizontal (estimated plunge in the 0–35° range), pointing toward a rough N-S orientation, while the σ_2 and σ_3 axes represent, alternatively, the vertical stress. In this region, only the σ_1 axis is well constrained by the inversion, while the σ_2 and σ_3 axes sometimes show a partial overlap of their estimated 95% confidence limits, suggesting that they are approximately equal in magnitude ($R > 0.75$). As a result, there are alternating sectors of the Himalayan Arc where σ_2 is sub-horizontal, like in most of the central Himalaya, and areas where it becomes vertical, such as in the Sikkim region, Himachal, and Bhutan. However, the σ_{Hmax} pattern along the Himalayan Arc effectively reflects the primary compression arising from the India–Eurasia convergence.

In Tibet, the best constrained stress axis is σ_3, which is always sub-horizontal with a W-E to NW-SE average strike. σ_1 and σ_2 axes are alternatively sub-vertical, with partial overlap of their estimated 95% confidence limits; therefore, they are approximately equal in magnitude ($R < 0.25$) and their possible flipping over the entire Tibet (Figure 6a) is admittable. Indeed, the flipping in the position of the σ_1 and σ_2 axes is consistent with the main features of active faults in the region (Figure 2). Tibet is currently deformed by both normal faults, which account for the vertical σ_1, and strike-slip faults, coherent with sub-horizontal σ_1 and σ_3.

Areas such as the central Tibetan region or the transition zone between the central Himalaya and Tibet are characterized by FMSs with heterogeneous kinematics, i.e., strike-slip, normal, and reverse faulting in the former and thrust (southward) and normal (northern) faulting in the latter, respectively. Despite these complex patterns, the achieved results are quite similar to the ones obtained for the neighboring cells, also evidencing an acceptable reliability for these estimations.

The σ_{Hmax} trajectories show a perpendicular trend with respect to the Himalayan Arc, mainly in the westernmost part, in the easternmost part of Nepal, and the Assam region (Figure 6a). The σ_{Hmax} on the Tibetan Plateau shows a pattern predominantly oriented along the N-S attitude till latitude 31°N. To the north, it rotates clockwise at approximately 30° and aligns NE-SW. This main direction can be observed northward, up to the Kunlun Fault. To the southeast, the σ_{Hmax} trajectories depict a clockwise rotation, passing from NW-SE to N-S and NE-SW above the Burma subduction system.

Figure 6b provides the spatial distribution of the estimated stress ratio (R) values. As previously mentioned, the stress ratio R varies from 0 ($\sigma_1 = \sigma_2$) to 1 ($\sigma_2 = \sigma_3$); therefore, in the following, we defined three main groups with $0.25 < R < 0.75$, $R \geq 0.75$ and $R \leq 0.25$. Regions with $0.25 < R < 0.75$ are sparsely distributed throughout the study area, generally lacking a distinct pattern and representing transitional values for the other two groups. Regions with $R < 0.25$ can be recognized across a large sector of Tibet, where, as pointed out before, σ_1 and σ_2 axes flip among them, evidencing that the crustal deformation is accommodated by the coexistence of active strike-slip and normal faults.

Regions with $R > 0.75$ are the Himalayan Arc, the area north of the Qaidam Basin and the northwest border of the Tarim Basin. In all these zones, the σ_1 axis is sub-horizontal, while σ_2 and σ_3 can alternatively represent the vertical stress, therefore evidencing the coexistence of the strike-slip and reverse faulting regimes.

5.3. Stress–Strain Comparison

The comparison of geodetic strain and seismological stress is carried out by comparing the azimuthal pattern of the ε_{Hmin} (shortening axis) and the σ_{Hmax} (maximum horizontal stress) (Figure 7). Strain and stress parameters have been estimated on grids with different sizes which, however, share several nodes; therefore, the comparison of their azimuthal

patterns has been performed by considering the estimated values at the shared nodes. A remarkable feature of this comparison is that, in 90% of cases, the estimated angular discrepancy is less than 15°, even in those regions where strain and stress axes show spectacular rotations (Figure 7). Considering uncertainties associated with both strain and stress fields (see Supplementary Material), the methodology used, the type of data, and their spatial distribution, these cases could be considered almost concordant. Based on this last consideration. This alignment is consistent with a macroscopically elastic mechanical response of the sampled upper crust, in which deformation tends to occur in the same direction as the applied stress. However, we acknowledge that this interpretation relies on a simplified model of isotropic elasticity, which may not apply in the presence of elastic anisotropy or more complex behaviors such as plasticity or viscoelasticity. At a regional scale, this correlation between the principal axes of stress and strain rate has been reported in previous studies [5,132]. Moreover, moderate-to-large azimuthal discrepancies can be recognized along the western (Himachal region) and eastern sectors of the Himalaya and along the NW border of the Tarim Basin, evidencing either a significant heterogeneity of the upper crust or the superposition of different stress sources.

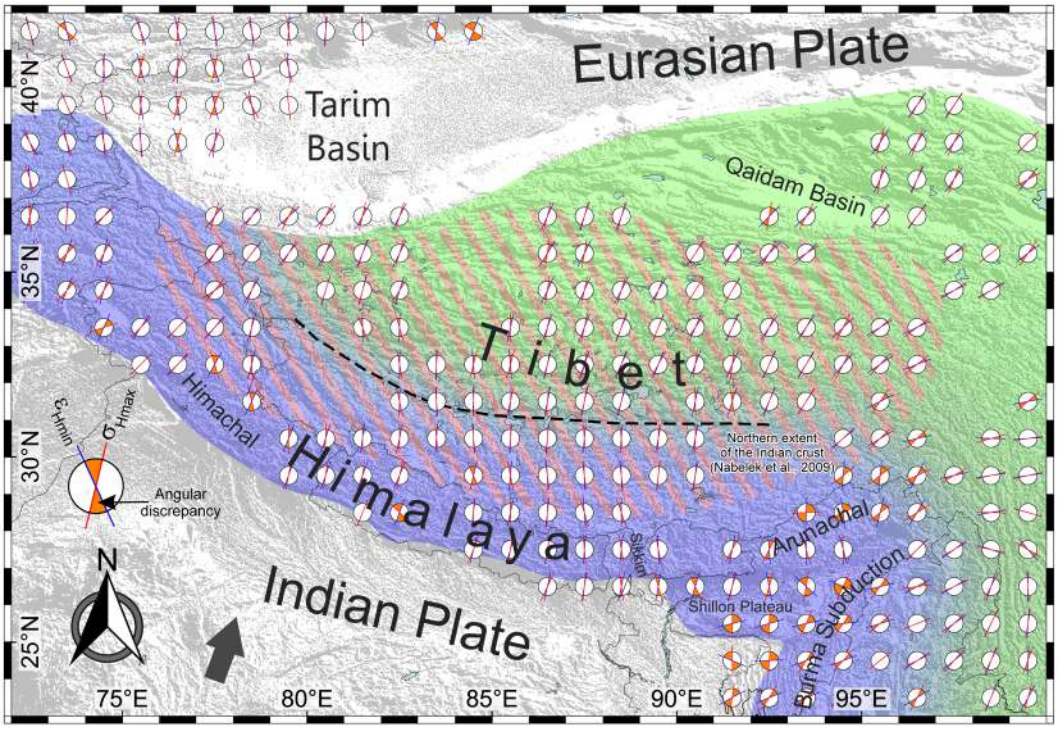

Figure 7. Azimuthal comparison between ε_{Hmin} in blue and σ_{Hmax} in red. The discrepancy angle between the horizontal axes is colored in orange. The northern limit of the underthrusted Indian crust [35] is marked by a black dashed line. Background colors are related to the zones largely affected by the suggested geodynamic models; the area mainly driven by escape tectonics [133] is reported in green, the area with the underthrusted Indian crust [35] is reported in blue, and the area affected by topographic loading is reported in red oblique strips. The black arrow stands for the relative India–Eurasia motion, as resulting from the analyzed GNSS data (Table S1 in Supplementary Materials). The terrain model is from GEBCO [30], accessed on 31 October 2024.

We also observe that along the Himalayan Arc, as well as the southern sector of the Tibetan Plateau, stress and strain azimuthal patterns are roughly sub-parallel to the predicted India–Eurasia relative motion (Figure 7). At a northern of latitude 31°N, the stress–strain azimuthal pattern shows a significant oblique relationship with the predicted one. We therefore suggest that the forces arising from the convergence process control both crustal stress and surface strain, at least along the southern sector of the orogenic belt. The

observed perturbation of this general pattern would be related to local complexities and/or to the superposition of secondary stress sources. Furthermore, the significant discrepancies between the observed stress and the predicted one northward of the 31° parallel provide significant evidence of a different driving mechanism that is actively shaping the ongoing tectonic setting of the Tibetan area.

6. Discussion and Conclusions

The compiled and analyzed database of GNSS data and earthquake focal mechanism solutions (see the Supplementary Material for details) allow an enhanced understanding of the kinematic zonation across the Himalaya–Tibet region. In particular, the computed GNSS velocity field, referred to the Eurasian reference frame [92], shows a fan-shaped feature (Figure 3) along the whole Himalayan Arc coupled with a large-scale clockwise rotation around the eastern sector of the Himalaya (Figure 4). Both features have been already detected by previous studies focusing on the area [88,134–137]. The fan-shaped feature along the Himalayan Arc effectively depicts the ongoing convergence between Indian and Eurasian plates, with rates decreasing northward, while the large-scale clockwise rotation appears related to deep processes involving the subducting lithosphere [88]. This computed GNSS velocity field has been used to estimate the horizontal strain-rate fields (Figure 5). The achieved results highlight a contractional pattern along the Himalayan orogeny, related to the India–Eurasia convergence. Tibet is prevalently deforming due to shear strain, coupled with a small fraction of crustal stretching, in agreement with Liu et al. [138]. Deformation in the inner part of the Tarim Basin is null, despite being currently trapped between the Altyn Tagh Fault and the Tianshan orogeny southward and northward, respectively. In such a context, the Tarim Basin behaves as a rigid block, as already suggested by Chang et al. [130] and Yang and Liu [131].

The reverse FMSs located along the Himalayan Arc, effectively suggests active thrusting occurring along the MHT (Figure 4). Reverse FMSs are also located along a roughly E-W oriented belt, extending from Pamir and Tian Shan to the west, up to the Qaidam Basin to the east. All these FMSs highlight the intense deformation accounted by the reverse faults, therefore evidencing that most of the convergence between Tarim and Eurasia is absorbed farther north, along the southern margin of the Kazakh platform, in central Asia [139]. FMSs with strike-slip features dominated the Tibetan Plateau, while numerous FMSs with normal faulting can also be observed. Abundant FMSs with strike-slip features can also be observed eastward of the Burma subduction zone. The achieved stress field is in agreement with previous studies [140] and highlights that along the Himalayan Arc, the σ_1 stress axis is roughly sub-horizontal with a prevailing N-S orientation, while the σ_2 and σ_3 axes represent, alternatively, the vertical stress, being both approximately equal in magnitude ($R > 0.75$). Conversely, the adjacent Tibetan region is experiencing both strike-slip and normal faulting, with the σ_3 being always sub-horizontal, with average strikes ranging from W-E to NW-SE, and the σ_2 and σ_1 axes approximately equal in magnitude ($R < 0.25$). The computed σ_{Hmax} trajectories (Figure 6a) show a main N-S orientation in both the Himalayan Arc and the southern part of Tibet, while at the latitude 31°N, the σ_{Hmax} orientations rotate toward a NE-SW strike. To the southeast, the σ_{Hmax} trajectories describe a large clockwise rotation, with orientations ranging from NW-SE to N-S and NE-SW above the Burma subduction system.

The azimuthal patterns of the geodetic shortening axis (ε_{Hmin}) and the seismological horizontal stress (σ_{Hmax}) have been compared by considering their estimates at the shared nodes of the computational grids. Over most of the study area, ε_{Hmin} and σ_{Hmax} are nearly parallel. Such a general alignment implies that the crust exhibits significant elasticity, as it is contracting along the σ_{Hmax} direction.

Novel stress–strain maps (Figures 5 and 6) provide new insights into the active geodynamic models suggested to explain the complex geodynamic setting of the Himalaya–Tibet region. We observed that stress and strain are roughly sub-parallel to the predicted motion of the India–Eurasia convergence, which therefore represents the main mechanism

in controlling both crustal stress and surface strain. Along the orogenic belt, the general pattern is locally modulated by some significant perturbations; considering available geological information along with our stress results we infer that these perturbations would be related to crustal lateral density changes, strength contrasts and active faults. Evidence of crustal lateral density changes and strength contrasts along the orogenic arc have been provided by local tomographic studies [141–143]. Moreover, along the Himalayan orogenic arc, the magnitude of ε_{Hmax} reveals several regions of arc-parallel stretching, consistent with the presence of N-S-oriented normal faults [144] and reoriented strike-slip faults [145,146]. Such a feature, coupled with the fan-shaped pattern of both ε_{Hmin} and σ_{Hmax} along the orogeny, aligns well with the *oblique convergence model* proposed by McCaffrey and Nábělek [26].

Along Tibet, we inferred small stress ratio values ($R \leq 0.25$), which suggests that at the local scale, σ_1 and σ_2 can act as the σ_{Hmax}. Given the close relationship between stress and strain, it can be inferred that the magnitude of the σ_{Hmax} axis is elastically proportional to the magnitude of the ε_{Hmin} axis, leading to a uniform distribution across Tibet (Figure 5c). This uniformity supports the idea that any variations in stress magnitude are more likely to occur along the vertical axis, rather than on the horizontal axis. Therefore, we propose that variation in the vertical stress is related to *topographic loading*, which would effectively modulate the stress related to the convergence process.

At the latitude of 31°N, our results show a ~30° rotation of the ε_{Hmin} and σ_{Hmax} axis. Such a boundary coincides at depth with the location of the northern extent of the underthrusted Indian Plate, as suggested by geophysical data [35,147]. At the surface, the boundary is not geologically well-defined; the normal and strike-slip faults [61,62,148] are quasi-homogeneously distributed at the scale of the whole Tibet. We therefore suggest that southern Tibet deforms in response to the stress field arising from the regional India–Eurasia convergence and local *topographic loading*, in agreement with the progressive underthrusting of the Indian Plate beneath southern Tibet. Conversely, in northern Tibet, the regional stress field related to the India–Eurasia convergence is largely modulated by the superposition of other stress sources.

Among the models proposed to explain the recent geodynamic evolution of the Tibetan region, the *indenter-escape tectonic* [25] model assumes that deformation is mainly confined to the horizontal plane and implies that compressive forces must be transmitted across plate boundaries, which in turn implies that the rate of the escaping must be equal to or less than the convergence rate. Moreover, this model also implies the eastward extrusion of Tibet. Such features can be easily observed on the GNSS-based velocity field (Figure 4), but limited toward the north of 31°N. Therefore, the *indenter-escape tectonic* model provides a plausible explanation of the motion of northern Tibet. However, it is unable to explain the vertical motion; therefore, other stress sources acting on the vertical component, such as the *topographic loading*, must be considered. Indeed, the combined action of both *indenter-escape tectonic* and *topographic loading* would provide a reasonable mechanism to properly explain the ongoing geodynamic evolution of this region.

An additional attempt to explain the complex deformation of the Himalaya–Tibet region was the *channel flow model* proposed by Bird [27]. This author hypothesized the presence of a deep zone in the Tibetan crust, hosting a planar channel flow which allowed the Himalayan Arc to expand both radially and circumferentially. However, our stress and strain trajectories do not support the *channel flow model*.

In conclusion, we support the combination of different geodynamic models, refining the model proposed by Copley et al. [149]. South of the 31°N latitude, compression is driven by basal drag from the underthrusting Indian Plate, while northward, escape tectonics dominate, where the eastward extrusion of the Tibetan Plateau becomes evident. All over Tibet, we can see no difference in terms of E-W stretching, leading to the idea that the normal faulting regime is due to *topographic loading*, given the uniform elevation of the plateau [24,149,150].

Geodetic and seismological data collected and analyzed in this study are provided as Supplementary Material so that they can be used as input for additional studies. Future

efforts should point toward an improved estimation of the crustal vertical motion, making this pattern a significant key element of the complex geodynamic processes of the Himalaya–Tibet region.

Supplementary Materials: The following supporting information can be downloaded at: https://www.mdpi.com/article/10.3390/rs16244765/s1, Table S1: catalog of Focal Mechanism Solutions with time, coordinates, magnitude, type of magnitude, depth, strike-dip-rake, reference and methods used, Table S2: site coordinates and velocities referred to ITRF14 and Eurasian reference frame for GNSS sites analyzed in the study area, Table S3: stress inversion results with an ID number, coordinates of the node, number of FMSs considered in the inversion, stress ratio (R), frictional coefficient, trend/plunge of the three principal axes (σ_1, σ_2 and σ_3), azimuth of the σ_{Hmax}, Table S4: geodetic strain rate node-by-node with azimuth, magnitude and uncertainties on ε_{Hmax}, ε_{Hmin} and dilatation, Figure S1: uncertainties in the calculation of node-by-node stress inversion, Georeferenced KML trajectory file S1: trajectories of the greatest contractional horizontal strain rate (ε_{Hmin}), same in Figure 5b, Georeferenced KML trajectory file S2: trajectories of the maximum horizontal stress (σ_{Hmax}), same in Figure 6a.

Author Contributions: Conceptualization F.P. and M.P.; methodology, F.P. and M.P.; software, F.P.; validation, F.P., M.P., A.M.-T. and G.L.; formal analysis, F.P.; investigation, E.S.; resources, M.P., A.S. and G.L.; data curation, F.P. and M.P.; writing—original draft preparation, F.P., M.P. and A.M.-T.; writing—review and editing, F.S., E.S., D.C., R.d.N., C.A., S.B., N.P. and A.S.; visualization, F.P.; supervision, M.P. and G.L.; project administration, G.L.; funding acquisition, M.P. and G.L. All authors have read and agreed to the published version of the manuscript.

Funding: A.M.T. is supported by the postdoctoral contract funded by the "Departamento de Educación del Gobierno Vasco" (Spain) (POS_2023_1_0001).

Data Availability Statement: Data are contained in the article and Supplementary Materials.

Acknowledgments: All the figures have been drawn by using GMT [151] tool and Inkscape (https://inkscape.org/ (accessed on 8 November 2024)) software.

Conflicts of Interest: The authors declare no conflicts of interest.

References

1. Rashidi, A.; Derakhshani, R. Strain and Moment Rates from GPS and Seismological Data in Northern Iran: Implications for an Evaluation of Stress Trajectories and Probabilistic Fault Rupture Hazard. *Remote Sens.* **2022**, *14*, 2219. [CrossRef]
2. Palano, M.; González, P.J.; Fernández, J. Strain and Stress Fields along the Gibraltar Orogenic Arc: Constraints on Active Geodynamics. *Gondwana Res.* **2013**, *23*, 1071–1088. [CrossRef]
3. Dobretsov, N.L.; Koulakov, I.Y.; Polyansky, O.P. Geodynamics and Stress–Strain Patterns in Different Tectonic Settings. *Russ. Geol. Geophys.* **2013**, *54*, 357–380. [CrossRef]
4. Reyners, M. Stress and Strain from Earthquakes at the Southern Termination of the Taupo Volcanic Zone, New Zealand. *J. Volcanol. Geotherm. Res.* **2010**, *190*, 82–88. [CrossRef]
5. Townend, J.; Zoback, M.D. Stress, Strain, and Mountain Building in Central Japan. *J. Geophys. Res.* **2006**, *111*, 2005JB003759. [CrossRef]
6. Chang, C.-P.; Chang, T.-Y.; Angelier, J.; Kao, H.; Lee, J.-C.; Yu, S.-B. Strain and Stress Field in Taiwan Oblique Convergent System: Constraints from GPS Observation and Tectonic Data. *Earth Planet. Sci. Lett.* **2003**, *214*, 115–127. [CrossRef]
7. Keiding, M.; Lund, B.; Árnadóttir, T. Earthquakes, Stress, and Strain along an Obliquely Divergent Plate Boundary: Reykjanes Peninsula, Southwest Iceland. *J. Geophys. Res.* **2009**, *114*, 2008JB006253. [CrossRef]
8. Van Hinsbergen, D.J.J.; Lippert, P.C.; Li, S.; Huang, W.; Advokaat, E.L.; Spakman, W. Reconstructing Greater India: Paleogeographic, Kinematic, and Geodynamic Perspectives. *Tectonophysics* **2019**, *760*, 69–94. [CrossRef]
9. Khattri, K.N.; Rogers, A.M.; Perkins, D.M.; Algermissen, S.T. A Seismic Hazard Map of India and Adjacent Areas. *Tectonophysics* **1984**, *108*, 93–134. [CrossRef]
10. Bhatia, S.C.; Kumar, M.R.; Gupta, H.K. A Probabilistic Seismic Hazard Map of India and Adjoining Regions. *Ann. Geophys.* **1999**, *42*. Available online: https://www.annalsofgeophysics.eu/index.php/annals/article/view/3777 (accessed on 18 December 2024).
11. Malik, J.N.; Srivastava, E.; Gadhavi, M.S.; Livio, F.; Sharma, N.; Arora, S.; Parrino, N.; Burrato, P.; Sulli, A. Holocene Surface-Rupturing Paleo-Earthquakes along the Kachchh Mainland Fault: Shaping the Seismic Landscape of Kachchh, Western India. *Sci. Rep.* **2024**, *14*, 11612. [CrossRef] [PubMed]

12. Srivastava, E.; Malik, J.N.; Parrino, N.; Burrato, P.; Sharma, N.; Gadhavi, M.; Sulli, A.; Di Maggio, C.; Morticelli, M.G. Extremely Fast Holocene Coastal Landscape Evolution in the Kachchh Upland (NW India): Clues from a Multidisciplinary Review. *J. Maps* **2023**, *19*, 2167617. [CrossRef]
13. Tian, X.; Chen, Y.; Tseng, T.-L.; Klemperer, S.L.; Thybo, H.; Liu, Z.; Xu, T.; Liang, X.; Bai, Z.; Zhang, X.; et al. Weakly Coupled Lithospheric Extension in Southern Tibet. *Earth Planet. Sci. Lett.* **2015**, *430*, 171–177. [CrossRef]
14. Bettinelli, P.; Avouac, J.-P.; Flouzat, M.; Jouanne, F.; Bollinger, L.; Willis, P.; Chitrakar, G.R. Plate Motion of India and Interseismic Strain in the Nepal Himalaya from GPS and DORIS Measurements. *J. Geod.* **2006**, *80*, 567–589. [CrossRef]
15. Bilham, R.; Larson, K.; Freymueller, J. GPS Measurements of Present-Day Convergence across the Nepal Himalaya. *Nature* **1997**, *386*, 61–64. [CrossRef]
16. Panda, D.; Lindsey, E.O. Overriding Plate Deformation Controls Inferences of Interseismic Coupling Along the Himalayan Megathrust. *JGR Solid Earth* **2024**, *129*, e2024JB029819. [CrossRef]
17. Kumar, P.; Malik, J.N.; Gahalaut, V.K.; Yadav, R.K.; Singh, G. Evidence of Strain Accumulation and Coupling Variation in the Himachal Region of NW Himalaya From Short Term Geodetic Measurements. *Tectonics* **2023**, *42*, e2022TC007690. [CrossRef]
18. Kumar, P.; Malik, J.N.; Gahalaut, V.K. Arc-Parallel Shear and Orogenic Deformation Along the Oblique Himalayan Convergent Plate Margin: Implications from Topographic- and Gradient-Anomaly Profiling in the Himalaya. *Pure Appl. Geophys.* **2023**, *180*, 2169–2189. [CrossRef]
19. Hetényi, G.; Cattin, R.; Berthet, T.; Le Moigne, N.; Chophel, J.; Lechmann, S.; Hammer, P.; Drukpa, D.; Sapkota, S.N.; Gautier, S.; et al. Segmentation of the Himalayas as Revealed by Arc-Parallel Gravity Anomalies. *Sci. Rep.* **2016**, *6*, 33866. [CrossRef]
20. De Sarkar, S.; Mathew, G.; Pande, K. Arc Parallel Extension in Higher and Lesser Himalayas, Evidence from Western Arunachal Himalaya, India. *J. Earth Syst. Sci.* **2013**, *122*, 715–727. [CrossRef]
21. Styron, R.; Taylor, M.; Sundell, K. Accelerated Extension of Tibet Linked to the Northward Underthrusting of Indian Crust. *Nat. Geosci.* **2015**, *8*, 131–134. [CrossRef]
22. Dasgupta, S.; Mukhopadhyay, B.; Mukhopadhyay, M.; Pande, P. Geo- and Seismo- Tectonics of Eastern Himalaya: Exploring Earthquake Source Zones from Foredeep to Tibetan Hinterland. *Phys. Chem. Earth Parts A/B/C* **2021**, *123*, 103013. [CrossRef]
23. Zhang, X.; Wang, Y. Seismic and GPS Evidence for the Kinematics and the State of Stress of Active Structures in South and South-Central Tibetan Plateau. *J. Asian Earth Sci.* **2007**, *29*, 283–295. [CrossRef]
24. Dewey, J.F. Extensional Collapse of Orogens. *Tectonics* **1988**, *7*, 1123–1139. [CrossRef]
25. Tapponnier, P.; Molnar, P. Slip-Line Field Theory and Large-Scale Continental Tectonics. *Nature* **1976**, *264*, 319–324. [CrossRef]
26. McCaffrey, R.; Nabelek, J. Role of Oblique Convergence in the Active Deformation of the Himalayas and Southern Tibet Plateau. *Geology* **1998**, *26*, 691. [CrossRef]
27. Bird, P. Lateral Extrusion of Lower Crust from under High Topography in the Isostatic Limit. *J. Geophys. Res.* **1991**, *96*, 10275–10286. [CrossRef]
28. Li, Y.; Wang, C.; Dai, J.; Xu, G.; Hou, Y.; Li, X. Propagation of the Deformation and Growth of the Tibetan–Himalayan Orogen: A Review. *Earth-Sci. Rev.* **2015**, *143*, 36–61. [CrossRef]
29. Zelenin, E.; Bachmanov, D.; Garipova, S.; Trifonov, V.; Kozhurin, A. The Active Faults of Eurasia Database (AFEAD): The Ontology and Design behind the Continental-Scale Dataset. *Earth Syst. Sci. Data* **2022**, *14*, 4489–4503. [CrossRef]
30. GEBCO Bathymetric Compilation Group. *The GEBCO_2023 Grid—A Continuous Terrain Model of the Global Oceans and Land*; GEBCO Bathymetric Compilation Group: Hurst, TX, USA, 2023.
31. Xiao, W.; Windley, B.F.; Sun, S.; Li, J.; Huang, B.; Han, C.; Yuan, C.; Sun, M.; Chen, H. A Tale of Amalgamation of Three Permo-Triassic Collage Systems in Central Asia: Oroclines, Sutures, and Terminal Accretion. *Annu. Rev. Earth Planet. Sci.* **2015**, *43*, 477–507. [CrossRef]
32. Zhu, R.; Zhao, P.; Zhao, L. Tectonic Evolution and Geodynamics of the Neo-Tethys Ocean. *Sci. China Earth Sci.* **2022**, *65*, 1–24. [CrossRef]
33. Bilham, R. Himalayan Earthquakes: A Review of Historical Seismicity and Early 21st Century Slip Potential. *Geol. Soc. Lond. Spec. Publ.* **2019**, *483*, 423–482. [CrossRef]
34. Molnar, P.; Tapponnier, P. Cenozoic Tectonics of Asia: Effects of a Continental Collision: Features of Recent Continental Tectonics in Asia Can Be Interpreted as Results of the India-Eurasia Collision. *Science* **1975**, *189*, 419–426. [CrossRef] [PubMed]
35. Nábělek, J.; Hetényi, G.; Vergne, J.; Sapkota, S.; Kafle, B.; Jiang, M.; Su, H.; Chen, J.; Huang, B.-S.; Team, T.H.-C. Underplating in the Himalaya-Tibet Collision Zone Revealed by the Hi-CLIMB Experiment. *Science* **2009**, *325*, 1371–1374. [CrossRef] [PubMed]
36. Rowley, D.B.; Currie, B.S. Palaeo-Altimetry of the Late Eocene to Miocene Lunpola Basin, Central Tibet. *Nature* **2006**, *439*, 677–681. [CrossRef]
37. Wu, Y.; Zheng, Z.; Nie, J.; Chang, L.; Su, G.; Yin, H.; Liang, H.; Pang, Y.; Chen, C.; Jiang, Z.; et al. High-Precision Vertical Movement and Three-Dimensional Deformation Pattern of the Tibetan Plateau. *JGR Solid Earth* **2022**, *127*, e2021JB023202. [CrossRef]
38. Powell, C.M. Continental Underplating Model for the Rise of the Tibetan Plateau. *Earth Planet. Sci. Lett.* **1986**, *81*, 79–94. [CrossRef]
39. Finch, M.; Hasalova, P.; Weinberg, R.F.; Fanning, C.M. Switch from Thrusting to Normal Shearing in the Zanskar Shear Zone, NW Himalaya: Implications for Channel Flow. *Geol. Soc. Am. Bull.* **2014**, *126*, 892–924. [CrossRef]
40. Wiesmayr, G.; Grasemann, B. Eohimalayan Fold and Thrust Belt: Implications for the Geodynamic Evolution of the NW-Himalaya (India). *Tectonics* **2002**, *21*, 8-1–8-18. [CrossRef]

41. Burchfiel, B.C.; Zhiliang, C.; Hodges, K.V.; Yuping, L.; Royden, L.H.; Changrong, D.; Jiene, X. The South Tibetan Detachment System, Himalayan Orogen: Extension Contemporaneous With and Parallel to Shortening in a Collisional Mountain Belt. In *Geological Society of America Special Papers*; Geological Society of America: Boulder, CO, USA, 1992; Volume 269, pp. 1–41, ISBN 978-0-8137-2269-6.
42. Aikman, A.B.; Harrison, T.M.; Lin, D. Evidence for Early (>44 Ma) Himalayan Crustal Thickening, Tethyan Himalaya, Southeastern Tibet. *Earth Planet. Sci. Lett.* **2008**, *274*, 14–23. [CrossRef]
43. Godin, L.; Grujic, D.; Law, R.D.; Searle, M.P. Channel Flow, Ductile Extrusion and Exhumation in Continental Collision Zones: An Introduction. *Geol. Soc. Lond. Spec. Publ.* **2006**, *268*, 1–23. [CrossRef]
44. Kellett, D.A.; Cottle, J.M.; Larson, K.P. The South Tibetan Detachment System: History, Advances, Definition and Future Directions. *Geol. Soc. Lond. Spec. Publ.* **2019**, *483*, 377–400. [CrossRef]
45. Hodges, K.V.; Burchfiel, B.C.; Royden, L.H.; Chen, Z.; Liu, Y. The Metamorphic Signature of Contemporaneous Extension and Shortening in the Central Himalayan Orogen: Data from the Nyalam Transect, Southern Tibet. *J. Metamorph. Geol.* **1993**, *11*, 721–737. [CrossRef]
46. Kellett, D.A.; Grujic, D. New Insight into the South Tibetan Detachment System: Not a Single Progressive Deformation. *Tectonics* **2012**, *31*, 2011TC002957. [CrossRef]
47. Jamieson, R.A.; Beaumont, C.; Nguyen, M.H.; Grujic, D. Provenance of the Greater Himalayan Sequence and Associated Rocks: Predictions of Channel Flow Models. *Geol. Soc. Lond. Spec. Publ.* **2006**, *268*, 165–182. [CrossRef]
48. Webb, A.A.G.; Schmitt, A.K.; He, D.; Weigand, E.L. Structural and Geochronological Evidence for the Leading Edge of the Greater Himalayan Crystalline Complex in the Central Nepal Himalaya. *Earth Planet. Sci. Lett.* **2011**, *304*, 483–495. [CrossRef]
49. Webb, A.A.G.; Yin, A.; Harrison, T.M.; Célérier, J.; Burgess, W.P. The Leading Edge of the Greater Himalayan Crystalline Complex Revealed in the NW Indian Himalaya: Implications for the Evolution of the Himalayan Orogen. *Geology* **2007**, *35*, 955. [CrossRef]
50. Dal Zilio, L.; Jolivet, R.; Van Dinther, Y. Segmentation of the Main Himalayan Thrust Illuminated by Bayesian Inference of Interseismic Coupling. *Geophys. Res. Lett.* **2020**, *47*, e2019GL086424. [CrossRef]
51. Ghoshal, S.; McQuarrie, N.; Robinson, D.M.; Adhikari, D.P.; Morgan, L.E.; Ehlers, T.A. Constraining Central Himalayan (Nepal) Fault Geometry Through Integrated Thermochronology and Thermokinematic Modeling. *Tectonics* **2020**, *39*, e2020TC006399. [CrossRef]
52. Dasgupta, S.; Mukhopadhyay, M.; Nandy, D.R. Active Transverse Features in the Central Portion of the Himalaya. *Tectonophysics* **1987**, *136*, 255–264. [CrossRef]
53. Bilham, R.; Gaur, V.K.; Molnar, P. Himalayan Seismic Hazard. *Science* **2001**, *293*, 1442–1444. [CrossRef] [PubMed]
54. Li, S.; Tao, T.; Gao, F.; Qu, X.; Zhu, Y.; Huang, J.; Wang, Q. Interseismic Coupling beneath the Sikkim–Bhutan Himalaya Constrained by GPS Measurements and Its Implication for Strain Segmentation and Seismic Activity. *Remote Sens.* **2020**, *12*, 2202. [CrossRef]
55. Michailos, K.; Carpenter, N.S.; Hetényi, G. Spatio-Temporal Evolution of Intermediate-Depth Seismicity Beneath the Himalayas: Implications for Metamorphism and Tectonics. *Front. Earth Sci.* **2021**, *9*, 742700. [CrossRef]
56. Coudurier-Curveur, A.; Tapponnier, P.; Okal, E.; Van Der Woerd, J.; Kali, E.; Choudhury, S.; Baruah, S.; Etchebes, M.; Karakaş, Ç. A Composite Rupture Model for the Great 1950 Assam Earthquake across the Cusp of the East Himalayan Syntaxis. *Earth Planet. Sci. Lett.* **2020**, *531*, 115928. [CrossRef]
57. Ben-Menahem, A.; Aboodi, E.; Schild, R. The Source of the Great Assam Earthquake—An Interplate Wedge Motion. *Phys. Earth Planet. Inter.* **1974**, *9*, 265–289. [CrossRef]
58. Galetzka, J.; Melgar, D.; Genrich, J.F.; Geng, J.; Owen, S.; Lindsey, E.O.; Xu, X.; Bock, Y.; Avouac, J.-P.; Adhikari, L.B.; et al. Slip Pulse and Resonance of the Kathmandu Basin during the 2015 Gorkha Earthquake, Nepal. *Science* **2015**, *349*, 1091–1095. [CrossRef]
59. Lindsey, E.O.; Natsuaki, R.; Xu, X.; Shimada, M.; Hashimoto, M.; Melgar, D.; Sandwell, D.T. Line-of-sight Displacement from ALOS-2 Interferometry: M_w 7.8 Gorkha Earthquake and M_w 7.3 Aftershock. *Geophys. Res. Lett.* **2015**, *42*, 6655–6661. [CrossRef]
60. Avouac, J.-P.; Ayoub, F.; Leprince, S.; Konca, O.; Helmberger, D.V. The 2005, Mw 7.6 Kashmir Earthquake: Sub-Pixel Correlation of ASTER Images and Seismic Waveforms Analysis. *Earth Planet. Sci. Lett.* **2006**, *249*, 514–528. [CrossRef]
61. Armijo, R.; Tapponnier, P.; Mercier, J.L.; Han, T. Quaternary Extension in Southern Tibet: Field Observations and Tectonic Implications. *J. Geophys. Res.* **1986**, *91*, 13803–13872. [CrossRef]
62. Taylor, M.; Peltzer, G. Current Slip Rates on Conjugate Strike-slip Faults in Central Tibet Using Synthetic Aperture Radar Interferometry. *J. Geophys. Res.* **2006**, *111*, 2005JB004014. [CrossRef]
63. Ryder, I.; Bürgmann, R.; Fielding, E. Static Stress Interactions in Extensional Earthquake Sequences: An Example from the South Lunggar Rift, Tibet. *J. Geophys. Res.* **2012**, *117*, 2012JB009365. [CrossRef]
64. Bie, L.; Ryder, I.; Nippress, S.E.J.; Bürgmann, R. Coseismic and Post-Seismic Activity Associated with the 2008 Mw 6.3 Damxung Earthquake, Tibet, Constrained by InSAR. *Geophys. J. Int.* **2014**, *196*, 788–803. [CrossRef]
65. Hu, X.; He, P.; Zhang, J. Source Mechanism of the 2020 Mw 6.3 Nima Earthquake Derived from Bayesian Inversions with InSAR Observations: Insight into E-W Extensional Activity in the Central Tibet. *Adv. Space Res.* **2022**, *70*, 1721–1736. [CrossRef]
66. Li, K.; Tapponnier, P.; Xu, X.; Ren, J.; Wang, S.; Zhao, J. Holocene Slip Rate Along the Beng Co Fault and Dextral Strike-Slip Extrusion of Central Eastern Tibet. *Tectonics* **2022**, *41*, e2022TC007230. [CrossRef]

67. Li, Q.; Li, C.; Tan, K.; Lu, X.; Zuo, X. Slip Model of the 2020 Yutian (Northwestern Tibetan Plateau) Earthquake Derived From Joint Inversion of InSAR and Teleseismic Data. *Earth Space Sci.* **2021**, *8*, e2020EA001409. [CrossRef]
68. Xie, C.; Lei, X.; Wu, X.; Hu, X. Short- and Long-Term Earthquake Triggering along the Strike-Slip Kunlun Fault, China: Insights Gained from the Ms 8.1 Kunlun Earthquake and Other Modern Large Earthquakes. *Tectonophysics* **2014**, *617*, 114–125. [CrossRef]
69. Harrison, T.M.; Copeland, P.; Kidd, W.S.F.; Yin, A. Raising Tibet. *Science* **1992**, *255*, 1663–1670. [CrossRef]
70. England, P.; Houseman, G. Extension during Continental Convergence, with Application to the Tibetan Plateau. *J. Geophys. Res.* **1989**, *94*, 17561–17579. [CrossRef]
71. Teng, J.; Deng, Y.; Badal, J.; Zhang, Y. Moho Depth, Seismicity and Seismogenic Structure in China Mainland. *Tectonophysics* **2014**, *627*, 108–121. [CrossRef]
72. Cao, J.; Shi, Y.; Zhang, H.; Wang, H. Numerical Simulation of GPS Observed Clockwise Rotation around the Eastern Himalayan Syntax in the Tibetan Plateau. *Sci. Bull.* **2009**, *54*, 1398–1410. [CrossRef]
73. Zhang, L.; Liang, S.; Yang, X.; Gan, W.; Dai, C. Geometric and Kinematic Evolution of the Jiali Fault, Eastern Himalayan Syntaxis. *J. Asian Earth Sci.* **2021**, *212*, 104722. [CrossRef]
74. Xu, Q.; Zhao, J.; Yuan, X.; Liu, H.; Pei, S. Detailed Configuration of the Underthrusting Indian Lithosphere Beneath Western Tibet Revealed by Receiver Function Images. *JGR Solid Earth* **2017**, *122*, 8257–8269. [CrossRef]
75. Shi, D.; Zhao, W.; Klemperer, S.L.; Wu, Z.; Mechie, J.; Shi, J.; Xue, G.; Su, H. West–East Transition from Underplating to Steep Subduction in the India–Tibet Collision Zone Revealed by Receiver-Function Profiles. *Earth Planet. Sci. Lett.* **2016**, *452*, 171–177. [CrossRef]
76. Zhang, Z.; Wang, Y.; Houseman, G.A.; Xu, T.; Wu, Z.; Yuan, X.; Chen, Y.; Tian, X.; Bai, Z.; Teng, J. The Moho beneath Western Tibet: Shear Zones and Eclogitization in the Lower Crust. *Earth Planet. Sci. Lett.* **2014**, *408*, 370–377. [CrossRef]
77. Kind, R.; Yuan, X.; Saul, J.; Nelson, D.; Sobolev, S.V.; Mechie, J.; Zhao, W.; Kosarev, G.; Ni, J.; Achauer, U.; et al. Seismic Images of Crust and Upper Mantle Beneath Tibet: Evidence for Eurasian Plate Subduction. *Science* **2002**, *298*, 1219–1221. [CrossRef]
78. Styron, R.H.; Taylor, M.H.; Sundell, K.E.; Stockli, D.F.; Oalmann, J.A.G.; Möller, A.; McCallister, A.T.; Liu, D.; Ding, L. Miocene Initiation and Acceleration of Extension in the South Lunggar Rift, Western Tibet: Evolution of an Active Detachment System from Structural Mapping and (U-Th)/He Thermochronology. *Tectonics* **2013**, *32*, 880–907. [CrossRef]
79. Panda, D.; Kundu, B.; Santosh, M. Oblique Convergence and Strain Partitioning in the Outer Deformation Front of NE Himalaya. *Sci. Rep.* **2018**, *8*, 10564. [CrossRef]
80. Styron, R.H.; Taylor, M.H.; Murphy, M.A. Oblique Convergence, Arc-Parallel Extension, and the Role of Strike-Slip Faulting in the High Himalaya. *Geosphere* **2011**, *7*, 582–596. [CrossRef]
81. Saylor, J.; DeCelles, P.; Gehrels, G.; Murphy, M.; Zhang, R.; Kapp, P. Basin Formation in the High Himalaya by Arc-Parallel Extension and Tectonic Damming: Zhada Basin, Southwestern Tibet. *Tectonics* **2010**, *29*. [CrossRef]
82. Beaumont, C.; Jamieson, R.A.; Nguyen, M.H.; Lee, B. Himalayan Tectonics Explained by Extrusion of a Low-Viscosity Crustal Channel Coupled to Focused Surface Denudation. *Nature* **2001**, *414*, 738–742. [CrossRef]
83. Copley, A.; McKenzie, D. Models of Crustal Flow in the India-Asia Collision Zone. *Geophys. J. Int.* **2007**, *169*, 683–698. [CrossRef]
84. Rey, P.F.; Teyssier, C.; Whitney, D.L. Limit of Channel Flow in Orogenic Plateaux. *Lithosphere* **2010**, *2*, 328–332. [CrossRef]
85. Herring, T.A.; Floyd, M.; Perry, M.; King, R.W.; McClusky, S.C. *2018—GAMIT-GLOBK for GNSS*; Massachusetts Institute of Technology: Cambridge, MA, USA, 2018; pp. 1–48.
86. Billi, A.; Cuffaro, M.; Orecchio, B.; Palano, M.; Presti, D.; Totaro, C. Retracing the Africa–Eurasia Nascent Convergent Boundary in the Western Mediterranean Based on Earthquake and GNSS Data. *Earth Planet. Sci. Lett.* **2023**, *601*, 117906. [CrossRef]
87. Altamimi, Z.; Rebischung, P.; Métivier, L.; Collilieux, X. ITRF2014: A New Release of the International Terrestrial Reference Frame Modeling Nonlinear Station Motions. *JGR Solid Earth* **2016**, *121*, 6109–6131. [CrossRef]
88. Wang, M.; Shen, Z. Present-Day Crustal Deformation of Continental China Derived From GPS and Its Tectonic Implications. *JGR Solid Earth* **2020**, *125*, e2019JB018774. [CrossRef]
89. Hao, M.; Li, Y.; Zhuang, W. Crustal Movement and Strain Distribution in East Asia Revealed by GPS Observations. *Sci. Rep.* **2019**, *9*, 16797. [CrossRef]
90. Frohling, E.; Szeliga, W. GPS Constraints on Interplate Locking within the Makran Subduction Zone. *Geophys. J. Int.* **2016**, *205*, 67–76. [CrossRef]
91. Sparacino, F.; Palano, M.; Peláez, J.A.; Fernández, J. Geodetic Deformation versus Seismic Crustal Moment-Rates: Insights from the Ibero-Maghrebian Region. *Remote Sens.* **2020**, *12*, 952. [CrossRef]
92. Altamimi, Z.; Métivier, L.; Rebischung, P.; Rouby, H.; Collilieux, X. ITRF2014 Plate Motion Model. *Geophys. J. Int.* **2017**, *209*, 1906–1912. [CrossRef]
93. Heidbach, O.; Rajabi, M.; Cui, X.; Fuchs, K.; Müller, B.; Reinecker, J.; Reiter, K.; Tingay, M.; Wenzel, F.; Xie, F.; et al. The World Stress Map Database Release 2016: Crustal Stress Pattern across Scales. *Tectonophysics* **2018**, *744*, 484–498. [CrossRef]
94. De La Torre, T.L.; Monsalve, G.; Sheehan, A.F.; Sapkota, S.; Wu, F. Earthquake Processes of the Himalayan Collision Zone in Eastern Nepal and the Southern Tibetan Plateau. *Geophys. J. Int.* **2007**, *171*, 718–738. [CrossRef]
95. Ali, S.M.; Shanker, D. Study of Seismicity in the NW Himalaya and Adjoining Regions Using IMS Network. *J. Seism. Seismol.* **2017**, *21*, 317–334. [CrossRef]
96. Bai, L.; Liu, H.; Ritsema, J.; Mori, J.; Zhang, T.; Ishikawa, Y.; Li, G. Faulting Structure above the Main Himalayan Thrust as Shown by Relocated Aftershocks of the 2015 M_w 7.8 Gorkha, Nepal, Earthquake. *Geophys. Res. Lett.* **2016**, *43*, 637–642. [CrossRef]

97. Chandra, U. Seismicity, Earthquake Mechanisms and Tectonics along the Himalayan Mountain Range and Vicinity. *Phys. Earth Planet. Inter.* **1978**, *16*, 109–131. [CrossRef]
98. Chen, W.; Molnar, P. Source Parameters of Earthquakes and Intraplate Deformation beneath the Shillong Plateau and the Northern Indoburman Ranges. *J. Geophys. Res.* **1990**, *95*, 12527–12552. [CrossRef]
99. Han, C.; Huang, Z.; Xu, M.; Wang, L.; Mi, N.; Yu, D.; Li, H. Focal Mechanism and Stress Field in the Northeastern Tibetan Plateau: Insight into Layered Crustal Deformations. *Geophys. J. Int.* **2019**, *218*, 2066–2078. [CrossRef]
100. Kayal, J.R.; Arefiev, S.S.; Baruah, S.; Hazarika, D.; Gogoi, N.; Gautam, J.L.; Baruah, S.; Dorbath, C.; Tatevossian, R. Large and Great Earthquakes in the Shillong Plateau–Assam Valley Area of Northeast India Region: Pop-up and Transverse Tectonics. *Tectonophysics* **2012**, *532*, 186–192. [CrossRef]
101. Kumar, A.; Mitra, S.; Suresh, G. Seismotectonics of the Eastern Himalayan and Indo-Burman Plate Boundary Systems: Seismotectonics of Northeast of India. *Tectonics* **2015**, *34*, 2279–2295. [CrossRef]
102. Luo, J.; Zhao, C.; Lü, J.; Zhou, L.; Zheng, S. Characteristics of Focal Mechanisms and the Stress Field in the Southeastern Margin of the Tibetan Plateau. *Pure Appl. Geophys.* **2016**, *173*, 2687–2710. [CrossRef]
103. Mukhopadhyay, M.; Dasgupta, S. Deep Structure and Tectonics of the Burmese Arc: Constraints from Earthquake and Gravity Data. *Tectonophysics* **1988**, *149*, 299–322. [CrossRef]
104. Nandy, D.R.; Dasgupta, S. Seismotectonic Domains of Northeastern India and Adjacent Areas. *Phys. Chem. Earth* **1991**, *18*, 371–384. [CrossRef]
105. O'Kane, A.; Copley, A.; Mitra, S.; Wimpenny, S. The Geometry of Active Shortening in the Northwest Himalayas and the Implications for Seismic Hazard. *Geophys. J. Int.* **2022**, *231*, 2009–2033. [CrossRef]
106. Parija, M.P.; Kumar, S.; Tiwari, V.M.; Rao, N.P.; Kumar, N.; Biswal, S.; Singh, I. Microseismicity, Tectonics and Seismic Potential in the Western Himalayan Segment, NW Himalaya, India. *J. Asian Earth Sci.* **2018**, *159*, 1–16. [CrossRef]
107. Paul, H.; Mitra, S.; Bhattacharya, S.N.; Suresh, G. Active Transverse Faulting within Underthrust Indian Crust beneath the Sikkim Himalaya. *Geophys. J. Int.* **2015**, *201*, 1072–1083. [CrossRef]
108. Rastogi, B.K. Earthquake Mechanisms and Plate Tectonics in the Himalayan Region. *Tectonophysics* **1974**, *21*, 47–56. [CrossRef]
109. Wang, X.; Wei, S.; Wu, W. Double-Ramp on the Main Himalayan Thrust Revealed by Broadband Waveform Modeling of the 2015 Gorkha Earthquake Sequence. *Earth Planet. Sci. Lett.* **2017**, *473*, 83–93. [CrossRef]
110. Yadav, D.K.; Kumar, N.; Hazarika, D.; Yadav, D.N.; Wadhawan, M. Seismicity and Tectonics of Kinnaur Himalaya and Adjoining Region Inferred from Focal Mechanism Solutions and Stress Tensor Inversion. *Himal. Geol.* **2017**, *38*, 49–55.
111. Zhu, L.; Helmberger, D.V. Intermediate Depth Earthquakes beneath the India-Tibet Collision Zone. *Geophys. Res. Lett.* **1996**, *23*, 435–438. [CrossRef]
112. Kusumawati, D.; Sahara, D.P.; Puspito, N.T.; Baskara, A.W.; Kurniawan, A.; Tanihaha, W.; Solihin, L.J.J.; Pratama, M.D.; Patimah, S.H.; Sasmi, A.T.; et al. Moment Tensor Inversion Implementation in Determining Focal Mechanism Solution of Palu-Koro and Matano Fault Events: Processing Strategy. *IOP Conf. Ser. Earth Environ. Sci.* **2023**, *1227*, 012043. [CrossRef]
113. Adinolfi, G.M.; De Matteis, R.; De Nardis, R.; Zollo, A. A Functional Tool to Explore the Reliability of Micro-Earthquake Focal Mechanism Solutions for Seismotectonic Purposes. *Solid Earth* **2022**, *13*, 65–83. [CrossRef]
114. Baruah, S.; Saikia, S.; Baruah, S.; Bora, P.K.; Tatevossian, R.; Kayal, J.R. The September 2011 Sikkim Himalaya Earthquake Mw 6.9: Is It a Plane of Detachment Earthquake? *Geomat. Nat. Hazards Risk* **2016**, *7*, 248–263. [CrossRef]
115. Zhang, Z.; Klemperer, S.; Bai, Z.; Chen, Y.; Teng, J. Crustal Structure of the Paleozoic Kunlun Orogeny from an Active-Source Seismic Profile between Moba and Guide in East Tibet, China. *Gondwana Res.* **2011**, *19*, 994–1007. [CrossRef]
116. Zoback, M.L. First- and Second-order Patterns of Stress in the Lithosphere: The World Stress Map Project. *J. Geophys. Res.* **1992**, *97*, 11703–11728. [CrossRef]
117. Shen, Z.; Wang, M.; Zeng, Y.; Wang, F. Optimal Interpolation of Spatially Discretized Geodetic Data. *Bull. Seismol. Soc. Am.* **2015**, *105*, 2117–2127. [CrossRef]
118. Palano, M.; Imprescia, P.; Agnon, A.; Gresta, S. An Improved Evaluation of the Seismic/Geodetic Deformation-Rate Ratio for the Zagros Fold-and-Thrust Collisional Belt. *Geophys. J. Int.* **2018**, *213*, 194–209. [CrossRef]
119. Nucci, R.; Serpelloni, E.; Faenza, L.; Garcia, A.; Belardinelli, M.E. Comparative Analysis of Methods to Estimate Geodetic Strain Rates from GNSS Data in Italy. *Ann. Geophys.* **2024**, *66*, DM531. [CrossRef]
120. Vavryčuk, V. Iterative Joint Inversion for Stress and Fault Orientations from Focal Mechanisms. *Geophys. J. Int.* **2014**, *199*, 69–77. [CrossRef]
121. Bott, M.H.P. The Mechanics of Oblique Slip Faulting. *Geol. Mag.* **1959**, *96*, 109–117. [CrossRef]
122. Wallace, R.E. Geometry of Shearing Stress and Relation to Faulting. *J. Geol.* **1951**, *59*, 118–130. [CrossRef]
123. Gephart, J.W.; Forsyth, D.W. An Improved Method for Determining the Regional Stress Tensor Using Earthquake Focal Mechanism Data: Application to the San Fernando Earthquake Sequence. *J. Geophys. Res.* **1984**, *89*, 9305–9320. [CrossRef]
124. Vavryčuk, V.; Bouchaala, F.; Fischer, T. High-Resolution Fault Image from Accurate Locations and Focal Mechanisms of the 2008 Swarm Earthquakes in West Bohemia, Czech Republic. *Tectonophysics* **2013**, *590*, 189–195. [CrossRef]
125. Lund, B.; Slunga, R. Stress Tensor Inversion Using Detailed Microearthquake Information and Stability Constraints: Application to Ölfus in Southwest Iceland. *J. Geophys. Res.* **1999**, *104*, 14947–14964. [CrossRef]
126. Michael, A.J. Determination of Stress from Slip Data: Faults and Folds. *J. Geophys. Res.* **1984**, *89*, 11517–11526. [CrossRef]

127. Lund, B.; Townend, J. Calculating Horizontal Stress Orientations with Full or Partial Knowledge of the Tectonic Stress Tensor. *Geophys. J. Int.* **2007**, *170*, 1328–1335. [CrossRef]
128. Ge, W.; Molnar, P.; Shen, Z.; Li, Q. Present-day Crustal Thinning in the Southern and Northern Tibetan Plateau Revealed by GPS Measurements. *Geophys. Res. Lett.* **2015**, *42*, 5227–5235. [CrossRef]
129. Milnes, A.G. Aspects of "Strike-Slip" or Wrench Tectonics an Introductory Discussion. *Nor. J. Geol.* **1994**, *74*, 129–133.
130. Chang, H.; An, Z.; Liu, W.; Ao, H.; Qiang, X.; Song, Y.; Lai, Z. Quaternary Structural Partitioning within the Rigid Tarim Plate Inferred from Magnetostratigraphy and Sedimentation Rate in the Eastern Tarim Basin in China. *Quat. Res.* **2014**, *81*, 424–432. [CrossRef]
131. Yang, Y.; Liu, M. Cenozoic Deformation of the Tarim Plate and the Implications for Mountain Building in the Tibetan Plateau and the Tian Shan. *Tectonics* **2002**, *21*, 9-1–9-17. [CrossRef]
132. Palano, M. On the Present-Day Crustal Stress, Strain-Rate Fields and Mantle Anisotropy Pattern of Italy. *Geophys. J. Int.* **2015**, *200*, 969–985. [CrossRef]
133. Tapponnier, P.; Peltzer, G.; Armijo, R. On the Mechanics of the Collision between India and Asia. *Geol. Soc. Lond. Spec. Publ.* **1986**, *19*, 113–157. [CrossRef]
134. Vernant, P.; Bilham, R.; Szeliga, W.; Drupka, D.; Kalita, S.; Bhattacharyya, A.K.; Gaur, V.K.; Pelgay, P.; Cattin, R.; Berthet, T. Clockwise Rotation of the Brahmaputra Valley Relative to India: Tectonic Convergence in the Eastern Himalaya, Naga Hills, and Shillong Plateau. *JGR Solid Earth* **2014**, *119*, 6558–6571. [CrossRef]
135. Gan, W.; Zhang, P.; Shen, Z.; Niu, Z.; Wang, M.; Wan, Y.; Zhou, D.; Cheng, J. Present-day Crustal Motion within the Tibetan Plateau Inferred from GPS Measurements. *J. Geophys. Res.* **2007**, *112*, 2005JB004120. [CrossRef]
136. Zhang, P.-Z.; Shen, Z.; Wang, M.; Gan, W.; Bürgmann, R.; Molnar, P.; Wang, Q.; Niu, Z.; Sun, J.; Wu, J.; et al. Continuous Deformation of the Tibetan Plateau from Global Positioning System Data. *Geology* **2004**, *32*, 809. [CrossRef]
137. Wang, Q.; Zhang, P.-Z.; Freymueller, J.T.; Bilham, R.; Larson, K.M.; Lai, X.; You, X.; Niu, Z.; Wu, J.; Li, Y.; et al. Present-Day Crustal Deformation in China Constrained by Global Positioning System Measurements. *Science* **2001**, *294*, 574–577. [CrossRef] [PubMed]
138. Liu, C.; Ji, L.; Zhu, L.; Xu, C.; Zhao, C.; Lu, Z.; Wang, Q. Kilometer-Resolution Three-Dimensional Crustal Deformation of Tibetan Plateau from InSAR and GNSS. *Sci. China Earth Sci.* **2024**, *67*, 1818–1835. [CrossRef]
139. Zubovich, A.V.; Wang, X.; Scherba, Y.G.; Schelochkov, G.G.; Reilinger, R.; Reigber, C.; Mosienko, O.I.; Molnar, P.; Michajljow, W.; Makarov, V.I.; et al. GPS Velocity Field for the Tien Shan and Surrounding Regions. *Tectonics* **2010**, *29*. [CrossRef]
140. Wei, J.; Weifeng, S.; Xiaojing, M. Tectonic Stress Pattern in the Chinese Mainland from the Inversion of Focal Mechanism Data. *J. Earth Syst. Sci.* **2017**, *126*, 41. [CrossRef]
141. Raoof, J.; Mukhopadhyay, S.; Koulakov, I.; Kayal, J.R. 3-D Seismic Tomography of the Lithosphere and Its Geodynamic Implications beneath the Northeast India Region. *Tectonics* **2017**, *36*, 962–980. [CrossRef]
142. Thirunavukarasu, A.; Kumar, A.; Mitra, S. Lateral Variation of Seismic Attenuation in Sikkim Himalaya. *Geophys. J. Int.* **2017**, *208*, 257–268. [CrossRef]
143. Mukhopadhyay, S.; Sharma, J. Attenuation Characteristics of Garwhal–Kumaun Himalayas from Analysis of Coda of Local Earthquakes. *J. Seism. Seismol.* **2010**, *14*, 693–713. [CrossRef]
144. Stevens, V.L.; Avouac, J.-P. On the Relationship between Strain Rate and Seismicity in the India–Asia Collision Zone: Implications for Probabilistic Seismic Hazard. *Geophys. J. Int.* **2021**, *226*, 220–245. [CrossRef]
145. Malik, J.N.; Arora, S.; Gadhavi, M.S.; Singh, G.; Kumar, P.; Johnson, F.C.; Thakur, M.; Raoof, J. Geological Evidence of Paleo-Earthquakes on a Transverse Right-Lateral Strike-Slip Fault along the NW Himalayan Front: Implications towards Fault Segmentation and Strain Partitioning. *J. Asian Earth Sci.* **2023**, *244*, 105518. [CrossRef]
146. Berthet, T.; Ritz, J.-F.; Ferry, M.; Pelgay, P.; Cattin, R.; Drukpa, D.; Braucher, R.; Hetenyi, G. Active Tectonics of the Eastern Himalaya: New Constraints from the First Tectonic Geomorphology Study in Southern Bhutan. *Geology* **2014**, *42*, 427–430. [CrossRef]
147. Van Hinsbergen, D.J.J. Indian Plate Paleogeography, Subduction and Horizontal Underthrusting below Tibet: Paradoxes, Controversies and Opportunities. *Natl. Sci. Rev.* **2022**, *9*, nwac074. [CrossRef] [PubMed]
148. Rothery, D.A.; Drury, S.A. The Neotectonics of the Tibetan Plateau. *Tectonics* **1984**, *3*, 19–26. [CrossRef]
149. Copley, A.; Avouac, J.-P.; Wernicke, B.P. Evidence for Mechanical Coupling and Strong Indian Lower Crust beneath Southern Tibet. *Nature* **2011**, *472*, 79–81. [CrossRef]
150. Rey, P.; Vanderhaeghe, O.; Teyssier, C. Gravitational Collapse of the Continental Crust: Definition, Regimes and Modes. *Tectonophysics* **2001**, *342*, 435–449. [CrossRef]
151. Wessel, P.; Luis, J.F.; Uieda, L.; Scharroo, R.; Wobbe, F.; Smith, W.H.F.; Tian, D. The Generic Mapping Tools Version 6. *Geochem. Geophys. Geosyst.* **2019**, *20*, 5556–5564. [CrossRef]